

1 **The protocataclasite dilemma: *in situ* ^{36}Cl and REE-Y lessons from an impure limestone**
2 **fault scarp at Sparta, Greece**

3
4 Bradley W. Goodfellow^{1,2,3,4}, Marc W. Caffee^{5,6}, Greg Chmiel⁵, Ruben Fritzon^{1,3#}, Alasdair
5 Skelton^{2,3}, Arjen P. Stroeven^{1,3*}

6
7 ¹Department of Physical Geography, Stockholm University, Stockholm, Sweden

8 ²Department of Geological Sciences, Stockholm University, Stockholm, Sweden

9 ³Bolin Centre for Climate Research, Stockholm University, Stockholm, Sweden

10 ⁴Geological Survey of Sweden, Killiansgatan 10, Lund, Sweden

11 ⁵Department of Physics and Astronomy/Purdue Rare Isotope Measurement Laboratory,
12 Purdue University, West Lafayette, USA

13 ⁶Department of Earth, Atmospheric, and Planetary Sciences, Purdue University, West
14 Lafayette, USA

15
16 *Corresponding author

17 Email: arjen.stroeven@natgeo.su.se

18 Phone: +46(0)8-16 4230

19 #Now at Celsiusskolan, Sporthallsvägen 7, 828 33 Edsbyn, Sweden

20

21

22 **Abstract**

23 Reconstructions of paleoseismicity are useful for understanding, and mitigating, seismic

24 hazard risks. We apply cosmogenic ^{36}Cl exposure-age dating and concentrations of rare-earth
25 elements and yttrium (REE-Y) to the paleoseismic history of the Sparta fault, Greece.

26 Bayesian-inference Markov chain Monte Carlo modeling of ^{36}Cl concentrations along a 7.2

27 m-long vertical profile on the Sparta Fault scarp at Anogia indicate an increase in average

28 slip rate of the scarp from 0.8–0.9 mm yr⁻¹ at 6.5–7.7 kyr ago to 1.1–1.2 mm yr⁻¹ up to the

29 devastating 464 B.C.E. earthquake. Average exhumation of the entire scarp up to the present

30 day is 0.7–0.8 mm yr⁻¹. Modelling does not indicate additional recent exhumation of the

31 Sparta fault after 464 B.C.E. The Sparta fault scarp is composed of fault breccia, containing

32 quartz and clay-lined pores, in addition to host rock-derived clasts of calcite and

33 microcrystalline calcite cement. The impurities control the distribution of REE-Y in the fault

34 scarp and contribute spatial variation to ^{36}Cl concentrations, which precludes the

35 identification of individual earthquakes that have exhumed the Sparta fault scarp from either

36 of these data sets. REE-Y may illustrate processes that localize slip to a discrete fault plane in

37 the Earth's near-surface but their potential use in paleoseismicity would benefit from further
38 evaluation.

39

40 **Keywords**

41 ³⁶Cl exposure dating; earthquake; limestone; normal fault; REE-Y; Sparta fault

42

43 **1 Introduction**

44 Seismic hazard risks are significant in many parts of the world and studying the magnitude,
45 recurrence, mechanisms, and impacts of past earthquakes helps form a basis for mitigating
46 current and future risk. While historical earthquake records are a crucial archive (Gürpınar,
47 2005), their spatial distribution is patchy and the recurrence interval of large earthquakes on
48 many faults predates historical records. Geologic-based inferences regarding earthquake
49 timing, recurrence intervals, and the magnitudes of slip and shaking intensity, are an essential
50 component of seismic hazard risk mitigation (McCalpin, 2009, p. 24). Topographic
51 expressions of tectonic faults, the displacement of surficial sediments revealed in trenches,
52 and geochemical alterations on subaerially exposed fault surfaces, may each provide evidence
53 useful to the study of paleoseismicity (e.g., Benedetti et al., 2002; Dramis and Blumetti,
54 2005; Michetti et al., 2005; Carcaillet et al., 2008; Manighetti et al., 2010; Mouslopoulou et
55 al., 2011; Smith et al., 2014; Cowie et al., 2017; Mozafari et al., 2022). Here we apply
56 concentrations of cosmic-ray-produced (cosmogenic) ³⁶Cl and rare-earth elements and
57 yttrium (REE-Y) to study paleoseismicity on the Sparta fault at Anogia, Greece (Fig. 1a, b).

58

59 The Mediterranean is a densely populated seismically active region subjected to 7360
60 earthquakes of magnitude (M) > 4 during 1998–2010 (Godey et al., 2013). Within the Aegean
61 tectonic plate (Fig. 1a), and around its margins, there were >1450 earthquakes during this

62 period, 77 of which were $M > 5$. In central Greece, earthquakes are associated with normal
63 faults, which occur because of extension of the Aegean plate (Jolivet et al., 2013). In
64 limestone, they may be identified by spectacular scarps, which form from the accumulation
65 of bedrock slip that occurs during successive earthquakes. Holocene fault scarps can be well-
66 preserved (Armijo et al., 1991), making them suitable targets for paleoseismic studies.

67

68 The concentration of cosmogenic ^{36}Cl (Zreda and Noller, 1998; Mitchell et al., 2001;
69 Benedetti et al., 2002; Palumbo et al., 2004; Schlagenhauf et al., 2010; Tesson et al., 2016;
70 Cowie et al., 2017; Iezzi et al., 2021; Mozafari et al., 2022) has been used to infer
71 paleoseismic activity in limestone normal faults. This nuclide is produced from spallogenic
72 and muonic reactions occurring in ^{40}Ca . Following an earthquake, the newly exposed scarp
73 segment accumulates ^{36}Cl , the concentration of which is dependent upon the duration of
74 subaerial exposure, potentially allowing the earthquake to be dated. However, because
75 earthquakes may be closely clustered in time (Bubeck et al., 2015) and the measured ^{36}Cl
76 concentrations may be consistent with a range of models (Goodall et al., 2021), a unique
77 unequivocal fit to a single model may not be possible. Accurately identifying individual
78 earthquakes is further challenged by ^{36}Cl concentrations along vertical profiles that deviate
79 from the theoretically predicted patterns. These deviations appear to be a ubiquitous feature
80 of normal faults developed in limestone (e.g., Benedetti et al., 2002; Palumbo et al., 2004;
81 Tesson et al., 2016; Cowie et al., 2017; Goodall et al., 2021; Mozafari et al., 2022; Dawood et
82 al., 2024). Collectively, these challenges have driven the development of more sophisticated
83 models for ^{36}Cl concentration profiles; for example Bayesian modeling incorporates prior
84 geologic information (Cowie et al., 2017; Beck et al., 2018; Tesson and Benedetti, 2019;
85 Tikhomirov et al., 2019; Goodall et al., 2021, Iezzi et al., 2021) with the goal of making more
86 robust inferences about past tectonic activity.

87

88 Fault scarps may be exhumed by earthquakes clustered within several thousands of years and
89 then lie dormant for similar, or even longer, periods (Wallace, 1987; Friedrich et al., 2003;
90 Benedetti et al., 2013, Cowie et al., 2017). Although this complicates the determination of
91 earthquake recurrence intervals, earthquake clusters followed by intervening quiescence may
92 may be discerned from fault scarp ^{36}Cl concentrations (Goodall et al., 2021). Exposure ages
93 from Holocene faults may provide information essential to determining the seismogenic
94 potential of a fault (Tesson et al., 2016).

95

96 Measurements of REE-Y have also been used to unravel paleoseismic information on
97 limestone fault scarps, frequently together with ^{36}Cl dating (Carcaillet et al., 2008; Manighetti
98 et al., 2010; Mouslopoulou et al., 2011; Tesson et al., 2016; Bello et al., 2023; Moraetis et al.,
99 2023). The distribution of REE-Y vertically along fault scarps may result from exchanges
100 with former hanging-wall soil REE-Y before uplift. REE-Y would be leached from
101 subaerially exposed scarp surfaces through calcite dissolution and accumulate in the surfaces
102 of the hanging wall soil where they form organic complexes (Carcaillet et al., 2008; Bello et
103 al., 2023; Moraetis et al., 2023). Because of low pH, calcite dissolution is highest where the
104 soil surface abuts the scarp and the REE-Y becomes locally enriched in the adjacent scarp
105 surface through soil-to-scarp REE-Y exchange during reprecipitation of calcite. Peaks in
106 REE-Y on fault scarp surfaces that are now subaerially exposed may therefore represent
107 former soil surfaces, which are now exposed to leaching and subsequent accumulation in the
108 hanging wall soil, thus completing a cycle. The spacing of these REE-Y peaks may permit
109 identification of the number of slip events and the vertical displacement lengths. These
110 inferences can be made independently of ^{36}Cl measurements. Using both techniques could
111 provide robust paleoseismic information for seismic risk assessment models.

112

113 The pioneering cosmogenic ^{36}Cl study of the Sparta fault by Benedetti et al. (2002) motivated
114 our studies. Benedetti et al. found evidence at Parori (Fig. 1b) for the historically recorded
115 464 B.C.E. earthquake that destroyed Sparta (Armijo et al., 1991) and five older earthquakes.
116 Interestingly, they were unable to substantiate a displacement from the historical 464 B.C.E.
117 earthquake at nearby Anogia. Our study objectives were to: (i) study slip rates on the Sparta
118 fault at Anogia, by taking advantage of recent advances in both the measurement of ^{36}Cl and
119 earthquake modelling, accounting for all ^{36}Cl production pathways and shielding effects
120 (Schlagenhauf et al., 2010), and Bayesian modelling using prior knowledge such as the 464
121 B.C.E. earthquake (Goodall et al., 2021); (ii) Complement the ^{36}Cl exposure dating with
122 measurements of REE-Y to best constrain the paleoseismic history of this fault.

123

124 **2 Geological Setting**

125 The Sparta fault is a 64 km long, NNW–SSE striking, range-bounding normal fault in
126 southern Peloponnese (Fig. 1a, b). It separates the eastern flank of the Taygetos Mountains
127 (maximum elevation of 2407 m a.s.l.) from the Sparta Basin (Fig. 1b). The Sparta fault is part
128 of a larger normal fault system, which exceeds 150 km in length, and is matched on the
129 western margin of the Taygetos Mountains by the antithetical Kalamata fault and other
130 similar faults located offshore of the Mani Peninsula (Fig. 1a; Armijo et al., 1991). The
131 subaerially exposed scarp of the Sparta fault is developed in late Senonian-Eocene limestones
132 of the Ionian unit (Institute for Geology and Subsurface Research, 1969; Armijo et al., 1991).
133 Folded and tilted Permian to early Triassic pelitic and psammitic sedimentary and
134 metasedimentary units outcrop in the Taygetos Mountains and are also offset by the Sparta
135 fault at depth (Institute for Geology and Subsurface Research, 1969; Armijo et al., 1991).
136 Geomorphic evidence for Quaternary uplift along the eastern flank of the Taygetos

137 Mountains includes steep triangular facets (20° – 40°) that are hundreds of meters high along
138 the central portion of the range and decrease in height towards the N and S, wineglass
139 canyons, perched valleys, and alluvial fans having up to 4 m of entrenchment near the Sparta
140 fault trace (Armijo et al., 1991; Benedetti et al., 2002; Pope and Wilkinson, 2005;
141 Papanikolaou et al., 2013). Collectively, the evidence indicates an environment that has been
142 tectonically active during the Holocene.

143

144 The Sparta fault scarp is nearly continuous along strike and it reaches a maximum height of
145 10–12 m in its central portion but tapers towards both ends. Hanging wall erosion associated
146 with stream incision can locally form higher scarp segments. The scarp has a 61 – 64° dip and,
147 in all but a few locations, slickensides have been eroded away following exhumation. The
148 slope of the hanging wall ground surface matches that upslope of the footwall, which
149 indicates a contiguous hillslope prior to formation of the present scarp and that sediment
150 accumulation at the scarp base is generally minor. Some wedges of sediment are locally
151 present on the hanging wall and in some places are welded to the scarp face, in positions now
152 perched above the hanging wall (Fig. S1). These wedges may have been perched by
153 earthquake-induced displacement on the Sparta fault or are debris deposits from mass
154 movements that have partly eroded. It is possible that other sediment wedges were also
155 formerly attached to the scarp face but have since fallen off.

156

157 Our sampling site is located at Anogia, where the Sparta fault scarp is 6.8 m high (Fig. 1c),
158 sparsely fractured, and displays a smooth surface texture (Fig. 1d-e). Apparent slickensides
159 are faintly visible as grooves that may have been widened and deepened by weathering, and
160 the surface displays a black coating, like those commonly occurring on limestone and which
161 contain higher concentrations of SiO_2 and Al_2O_3 than the underlying rock (Carcaillet et al.,

162 2008). The scarp surface at Anogia also displays a spatially variable distribution of subaerial
163 weathering features such as rills and dissolution pits, which we avoided in our sampling. The
164 lower-angle hillslopes on both the foot wall (above the fault scarp) and hanging wall display
165 a patchy distribution of bedrock outcrops and an indurated allochthonous regolith composed
166 of limestone clasts, with a matrix of red aeolian dust and calcite cement. An outcrop of
167 limestone about 50 m upslope of the fault scarp reveals folded and tilted bedding. The
168 bedding nearest to the scarp has a dip of 45–60° and a strike of 268–279°, which corresponds
169 with those for the fault scarp, indicating that faulting appears to exploit these structural
170 weaknesses in the bedrock. We neither observed scarps with a total offset of 2–3 m within
171 tens of meters downslope of the Sparta fault scarp (Benedetti et al., 2002), nor observed fault
172 scarps within hundreds of meters upslope of the Sparta fault scarp. If earthquakes, including
173 at 464 B.C.E., bypassed the fault scarp at Anogia (Benedetti et al., 2002), they did not leave
174 geomorphic expressions that we observed on field reconnaissance.

175

176

177 **3 Methods**

178 To study the paleoseismicity of the Sparta fault, we combined Accelerated Mass
179 Spectrometry (AMS) measurements of cosmogenic ³⁶Cl concentrations from samples
180 collected from the Sparta fault scarp with field and laboratory analyses of scarp composition
181 and mineralogy, and with field measurements of hanging wall soil composition and pH. We
182 made these measurements by sampling a vertical ³⁶Cl profile at Anogia, upwards from the
183 ground surface and adjacent to the sampling transect of Benedetti et al. (2002) for direct
184 comparison with that pre-existing record (Fig. 1c). We also took samples for ³⁶Cl and
185 mineralogical analyses, including REE-Y, from a second vertical profile located about 50 m
186 to the south (Fig. 1c). We chose this additional site for its smooth, non-fractured, fault scarp

187 surface, and sampling was completed from the top of the scarp to 80 cm below the present
188 ground surface, following hand excavation of a pit.

189

190 **3.1 ³⁶Cl concentrations**

191 We sampled the first profile (Anogia A), adjacent to the southern margin of the Benedetti et
192 al. (2002) profile, for ³⁶Cl by using an angle grinder to cut 10*20*3 cm (*h*w*d*) slabs from
193 the ground surface to a height of 3.9 m (Fig. 1c, d). Because of a crack in the fault scarp at
194 1.1 m above the ground, the transect was shifted laterally (towards the north) by 40 cm, thus
195 duplicating the measurement at 1.1 m. A total of 37 samples from this profile were measured
196 for ³⁶Cl concentration. We sampled the second profile (Anogia B), ~ 50 m further to the
197 south, for ³⁶Cl and mineralogical analyses initially by drilling 14 cores of 4 cm diameter to a
198 depth of 3 cm into the scarp surface (Fig. 1c, e). Four of these cores were spaced at 20 cm
199 intervals below the ground surface and eight were spaced at 80 cm intervals above the ground
200 surface to a height of 6.4 m, which is 0.4 m below the top of the scarp. These samples were
201 augmented by another two drill core samples at 1.2 m and at 6.0 m. Subsequently, we took 20
202 samples from this profile using an angle grinder to cut 10*20*3 cm (*h*w*d*) slabs from the
203 ground surface to a height of 2.0 m (Fig. 1c). A total of 71 samples from the three profiles
204 were subjected to preparation chemistry for ³⁶Cl targets and measured using AMS.

205

206 For ³⁶Cl measurements, limestone samples were crushed to approximately 0.5 mm diameter
207 and the whole sample was used without removing any size fraction through sieving. Prior to
208 partial dissolution approximately 120 g of crushed material was washed with deionized water
209 to remove fines. Following Stone et al. (1996), meteoric ³⁶Cl was removed using two cycles
210 of partial dissolution with nitric acid to dissolve 5% (by mass) of the carbonate each time. To
211 prepare the AMS target we used 30 g of dried sample, spiked with 1 mg of ³⁵Cl-enriched

212 sodium chloride carrier (Source: Icon Isotopes, ^{35}Cl 99.635 atom %, $^{35}\text{Cl}/^{37}\text{Cl} = 273$) to
213 measure native chloride by isotope dilution. A slurry of the sample and 120 g of deionized
214 water was slowly dissolved with 60 g of concentrated trace-metal grade nitric acid. Post-
215 dissolution, both liquid and undissolved solids were quantitatively transferred to a centrifuge
216 bottle where the solids were removed by centrifugation. The supernatant was decanted to
217 another centrifuge bottle and chloride was precipitated using one molar silver nitrate. After a
218 settling period, the bottle was centrifuged to isolate the silver chloride which was then
219 washed, dissolved with ammonium hydroxide, and treated with barium nitrate to remove
220 sulfate in preparation for further purification by chromatography. The solution was loaded
221 onto 5 ml of Bio-Rad AG 1-X8 strong anion-exchange resin and chloride was moved through
222 with 0.50 mmol, and then 0.150 mmol, nitric acid. After re-precipitation with silver nitrate
223 and a washing step the silver chloride was dried and packed into silver bromide-cored copper
224 holders. AMS measurements were performed at the Purdue Rare Isotope Measurement
225 Laboratory according to procedures in Muzikar et al. (2003); standards used for the
226 measurement are described in Sharma et al. (1990).

227

228 *3.1.1 Bayesian modelling of ^{36}Cl concentrations*

229 We apply the Bayesian Markov chain Monte Carlo (MCMC) code from Goodall et al. (2021)
230 to identify slip rates from ^{36}Cl concentrations. MCMC builds upon ‘modelscarp’ from
231 Schlagenhauf et al. (2010), which models the number of earthquakes, their ages, and resulting
232 displacements from ^{36}Cl concentrations based on user-defined inputs. ‘Modelscarp’ accounts
233 for each ^{36}Cl production pathway in limestone (Table 1 in Schlagenhauf et al., 2010). The
234 Goodall et al. (2021) MCMC code is adapted from Cowie et al. (2017) to generate potential
235 slip histories.

236

237 The MCMC code models: (i) scarp age, which is the timing of the earthquake to exhume the
238 uppermost, and therefore oldest, part of the fault scarp; (ii) time at which each subsequent
239 earthquake occurred and the corresponding height of exhumed scarp, and; (iii) time since the
240 most recent earthquake exhumed the lowest part of the fault scarp (elapsed time). The
241 exhumation of the entire scarp is attributed to a user-defined number of earthquakes that each
242 exhumed the same vertical length of scarp. The timing of each earthquake, apart from the
243 first and last, is dependent on the selected number of earthquakes. We follow Goodall et al.
244 (2021) in using the flexible change point method of Cowie et al. (2017), which allows for
245 variable slip rates between iterations.

246

247 We parametrized the MCMC model as follows. (i) We defined the scarp age as 8000 years
248 with a 1σ normally distributed prior of 1500 years. This selection is partly based on the
249 record that contemporary faults scarps in the Mediterranean region are Holocene in age. They
250 have been exhumed since the last glacial maximum (LGM) because hillslope bedrock erosion
251 and regolith transport rates were much higher during the LGM (e.g., more than ten times
252 higher for the Magnola Fault in Italy; Tucker et al., 2011), preventing ruptured fault scarps
253 from persisting as subaerially exposed features (e.g., Benedetti et al., 2002; Cowie et al.,
254 2017; Goodall et al., 2021). The adopted scarp age is refined as a consequence of fitting a
255 modelled ^{36}Cl concentration profile to the measured ^{36}Cl concentration profile using the
256 ‘modelscarp’ code of MCMC. The scarp age is also balanced by the period of pre-exposure,
257 which is the ^{36}Cl inventory that accumulated in the bedrock while it was mantled by a up to a
258 few meters of colluvium before initial post-LGM subaerial exposure. A wide Gaussian prior
259 (5000–16 000 years), is assigned in our modeling to account for the uncertainty in scarp age.
260 (ii) The elapsed time is defined as 2500 years, based on the youngest known earthquake on
261 the Sparta Fault of 464 B.C.E. We assign a 1σ uncertainty of 1000 years to reflect uncertainty

262 in the historical record. (iii) To further define the most likely slip rate history for the Sparta
263 fault, we completed multiple model runs with varying number of earthquakes (three to six)
264 and ^{36}Cl spallation production rates (48.8 ± 3.5 to 59.4 ± 4.3 atoms g Ca^{-1} yr $^{-1}$). These end-
265 member production rates are from Stone et al. (1996) and Schlagenhauf et al. (2010)
266 calculated from Lifton et al., (2005), respectively. All model runs used the temporally
267 variable geomagnetic field of Lifton et al. (2005) to scale the ^{36}Cl spallation production rate
268 and spallation production rates for K, Ti, and Fe are as shown in Table 1 from Schlagenhauf
269 et al. (2010). Scarp age and elapsed time are the priors in the MCMC model, the number of
270 earthquakes defines the timing and location on the scarp of slip change points, and prior
271 probabilities are as defined in the Goodall et al. (2021) MCMC code.

272

273 The MCMC algorithm generates a slip history, using the input parameters conditioned on
274 prior probability, to construct a forward model of ^{36}Cl concentrations for this slip history
275 (Goodall et al., 2021). The quality of the slip history solution is then assessed by comparing
276 modelled and measured ^{36}Cl concentration profiles. The algorithm iteratively adjusts a
277 parameter defining the slip history and recalculates a new forward model solution.

278 Acceptance of the new slip history hinges on either its likelihood surpassing that of the prior
279 model or the ratio of new to current likelihood exceeding a randomly selected value from a
280 uniform distribution between zero and one. Otherwise, the new model solution is discarded,
281 adhering to the principles of the Metropolis-Hastings algorithm (Metropolis et al., 1953;
282 Hastings, 1970). We ran this process for 200 000 iterations, using the parameters in Table 1,
283 and results were assessed on 160 000 iterations after a burn-in phase of 40 000 iterations were
284 excluded to mitigate the influence of initial parameters.

285

286 **3.2 Sparta fault scarp composition**

287 Fault scarp chemical composition and mineralogy were analyzed from Anogia B as follows.
288 An initial elemental analysis was done in the field on the Sparta fault scarp surface using an
289 Olympus Innov-X Delta (40 kV) handheld X-ray fluorescence (XRF) device. This instrument
290 performs elemental analyses with a circular sample spot of 8 mm diameter and can measure
291 elements heavier than Na. All elements lighter than Mg are reported as lighter elements (LE).
292 Of the elements that compose REE-Y, it was only capable of measuring yttrium. Sampling
293 was done at an interval of 5 cm (or less) over a 7.7 m vertical profile, beginning ~0.9 m
294 below the hanging wall soil surface. This profile corresponds with the location of the drill
295 core and 2.0 m-long ^{36}Cl profiles at Anogia B but was measured before either drilling or slab
296 sampling (Fig. 1c).

297

298 For more detailed analyses of elements, including REE-Y, a total of 39 cores (22 mm and 35
299 mm diameters and to depths of ~3 cm) were collected every 20 cm from a vertical transect at
300 Anogia B using a portable drill (Fig. 1d). The outermost 1 mm was removed from each core
301 prior to crushing to avoid contamination from the black surface coating. The next 15 mm of
302 each core were then rinsed with cold water, air dried, and crushed using a grinder with a steel
303 mortar to a grain size of $<100\ \mu\text{m}$. This crushing technique might supply additional REE-Y to
304 samples (Hickson and Juras, 1986) but if so, this likely occurs systematically across samples
305 and we are more interested in spatial trends, which we confirm independently using the
306 handheld XRF, than absolute abundances. The crushed samples were then analyzed for major
307 and trace elements using fusion inductively coupled plasma mass spectrometry (FUS-ICP-
308 MS) at Activation Laboratories (Ontario, Canada).

309

310 We complemented the FUS-ICP-MS analyses with spot elemental analysis of one rock core
311 from 1.1 m above the scarp base at Anogia B to make a high-resolution determination of any

312 spatial variations in the scarp composition. This was done with an energy-dispersive X-ray
313 spectroscope (EDS) attached to an environmental scanning electron microscope (ESEM). We
314 used a Quanta FEG 650 with Oxford-Inka EDS, and the analysis was made in a high-vacuum
315 environment at 20 kV. The technique is incapable of detecting REE-Y because their
316 concentrations are too low. Photomicrographs and backscatter images of pore spaces were
317 also taken using the ESEM. These analyses were completed at the Department of Geological
318 Sciences, Stockholm University.

319

320 **3.3 Sparta fault scarp mineralogy**

321 A modal analysis of mineral fractions was completed on thin sections taken from the
322 remaining 38 core samples. This was done by counting 1000 points on each thin section
323 (Hutchison, 1974) using a Pelcon automatic point counter attached to a Leica (DM LSP)
324 optical microscope. This point counter comprises a stepping frame attached to a control box
325 (power supply) and is also connected to a computer for statistical analyses using Pelcon
326 software version 2. The point counting and mineral identification was made using an
327 objective working distance of 1.52 mm. The line section pre-set step-length was 0.3 mm and
328 the line section distance was 1.5–2 mm. The point counting permitted a detailed quantitative
329 analysis of the mineralogy of the Sparta fault scarp surface. This detailed mineralogy was
330 then compared with the chemical composition data to determine whether phases other than
331 the host limestone are present.

332

333 **3.4 Hanging wall soil chemistry and pH**

334 Soil chemistry and pH were measured in samples taken at ~10 cm intervals to a depth of ~90
335 cm in the pit excavated at the base of the Anogia B profile (Fig. 1c). The elemental analysis
336 was again done with the handheld XRF device. Indicator strips were used to measure pH

337 from mixtures of 1:1 mass ratio of soil:distilled water, and soil:1 M KCl (Sikora and Moore,
338 2014). These analyses help determine the vertical distribution of REE-Y in the soil (using
339 yttrium as a proxy) and indicate how they might correlate with pH and the vertical
340 distribution of REE-Y in the fault scarp below the soil surface.

341

342 **4 Results**

343 **4.1 Sparta fault ^{36}Cl concentrations**

344 The cosmogenic nuclide ^{36}Cl concentrations from our three profiles (Table S1) and the
345 original Benedetti et al. (2002) ^{36}Cl concentrations are compared in Figure 2. The Anogia A
346 and Anogia B profiles display corresponding trends of increasing ^{36}Cl concentrations with
347 increasing height on the fault scarp. Only at 1.6 m do the trends strongly deviate from each
348 other. The Anogia B profile indicates generally lower ^{36}Cl concentrations including six of 19
349 points that do not overlap within uncertainty with data points at corresponding elevations on
350 the Anogia A profile. Four of those points are located from 1.0 m to 1.3 m. In comparison
351 with Anogia A, the adjacent segment of the Benedetti et al. (2002) profile (0–4 m) shows ^{36}Cl
352 concentrations that are on average 19% higher. Uncertainties (1σ) for data points comprising
353 each profile are almost identical, displaying a mean of 3.8% for the Benedetti et al. (2002)
354 profile versus 3.9% for the Anogia A and Anogia B profiles. However, the Benedetti et al.
355 (2002) profile displays more variation between adjacent sample points than is evident in our
356 profiles. Whereas concentrations differ between the three longest profiles, they show a
357 consistent gradient up to ~4 m on the scarp. Above 4 m on the scarp, both our Anogia B drill-
358 core profile and the Benedetti et al. (2002) profile display matching lower gradients. Whereas
359 differences in measured concentrations between our two profiles and the Benedetti et al.
360 (2002) profile might be expected given technical advances between measurements,
361 successive samples in our data display inconsistent variations between the Anogia A and B

362 profiles, despite them being horizontally separated by only ~ 50 m. This inability to replicate
363 measurements along two adjacent profiles justifies a focus on identifying slip rates using the
364 Goodall et al. (2021) model, rather than individual earthquakes, also because up-scarp ^{36}Cl
365 concentration gradients are more consistent between the profiles.

366

367 Slips rates for the Sparta fault are explored through comparing scarp exhumation generated
368 by three, five, and six modelled earthquakes, where each earthquake exhumes 183 cm, 122
369 cm, and 104 cm, respectively. We focus our analyses on the Anogia A profile supplemented
370 with drill core samples from above 3.9 m on the scarp and from the scarp surface buried by
371 colluvium. This combined profile was chosen for modelling both because the Anogia A
372 profile was sampled at 10 cm intervals up to 3.9 m on the scarp, versus only 2.1 m for Anogia
373 B, and because Anogia A is located adjacent to the Benedetti et al. 2002 profile. Furthermore,
374 MCMC modelling of ^{36}Cl concentrations did not converge with measured concentrations for
375 the full Anogia B profile (i.e., including the drill core samples above 2.1 m), but rather only
376 for the intensively sampled lowermost 2.1 m plus subsurface drill core samples. Modelling
377 only the lowermost 2.1 m plus subsurface drill core samples necessitated changes to scarp
378 age and preexposure from those used for the Anogia A plus drill core sample profile, because
379 this lowermost part of the scarp has a younger age, and to slip length because the 2.1 m profile
380 length is indivisible into the 6.5 m length of the Anogia A plus drill core sample profile.

381 These changes, especially to scarp age, invalidate comparisons of slip rates between the two
382 profiles, which are the focus of this paper. We did not measure compositions for the Anogia
383 A samples, so we use a mean scarp composition from Anogia B in our modelling. Results
384 from the Goodall et al. (2001) model applied to the Anogia A plus drill core profile are
385 shown below and in Figure S2, respectively, for end-member ^{36}Cl production rates of $59.4 \pm$
386 $4.3 \text{ atoms g Ca}^{-1} \text{ yr}^{-1}$ from Schlagenhauf et al. (2010) calculated from Lifton et al., (2005) and

387 48.8 ± 3.5 atoms g $\text{Ca}^{-1} \text{yr}^{-1}$ from Stone et al. (1996). Geochemical data for the fault scarp
388 used in modelling are shown in Table S2. Modelling results from Anogia B (lowermost 2.1 m
389 and subsurface drill core samples and the entire profile) are shown in Figure S3.

390

391 The results of the Bayesian inference MCMC modelling of ^{36}Cl data from the Sparta fault are
392 shown in Figures 3–5. The accepted scarp exhumation models ($n = 160\,000$) are shown in
393 slip versus time histograms (Fig. 3a). The maximum a posteriori probability (MAP) model,
394 shown by the red line, deviates slightly from the maximum model density (mean model,
395 black line) for each slip segment, but more so for the slip segment at 4.9–6.1 m on the scarp.
396 It indicates three exhumation events between 2.4 and 6.1 m on the scarp, that are closely
397 spaced in time at 5000–6000 years ago. The 95% confidence intervals (Fig. 3b) illustrate little
398 change in variance between model results from lower, younger parts of the scarp to older,
399 higher parts of the scarp, although the MAP model deviates towards being younger than the
400 mean model towards the top of the scarp. The range of accepted models fits the measured
401 ^{36}Cl data well (Fig. 3c) but accommodates a broad range of corresponding slip histories along
402 the entire vertical length of the scarp (Fig. 3d).

403

404 Statistics for how well the MCMC modelling fits the measured ^{36}Cl data and our initial
405 estimates of scarp age (8000 years) and elapsed time (2500 years) are illustrated in Figure 4
406 and summarized in Table S2. The posterior probability distribution function indicates that the
407 elapsed time since the most recent earthquake is consistent with the 464 B.C.E. earthquake
408 (mean of 2501 ± 164 years; Fig. 4a). In contrast, the time when the scarp started to form
409 (scarp age), presumably through a decrease in hillslope erosion following the LGM, is
410 indicated by the posterior probability distribution to have been longer than our initial estimate
411 of 8000 years (mean of 8742 ± 502 years; Fig. 4b). Mean values of likelihood, weighted

412 mean root square (RMS_w) and corrected Akaike's Information Criterion (AIC_c) are 0.25–
413 0.28, 13.9–14.6, and 863–893, respectively, across the modelled range of the number of slip
414 events (Figs. 4d and 4e; Table S2), indicating that the number of earthquakes (change points)
415 has minor influence on modelling a fit to measured ^{36}Cl concentrations.

416

417 The slip rate for the Sparta Fault is calculated from the most probable of models (i.e., the top
418 6.25% of fits to the ^{36}Cl data ($n = 10\,000$); Fig. 5, Table 2). For the entire vertical length of
419 the fault scarp, and five modelled earthquakes, both the mean and MAP slip rates are 0.7–0.8
420 mm yr^{-1} for end-member ^{36}Cl production rates, calculated up to the present day (Fig. 5a). For
421 the same calculation but excluding the 2500 year since the most recent known earthquake at
422 464 B.C.E., the slip rates are higher, with mean and MAP values of 1.1 and 1.2 mm yr^{-1} ,
423 respectively (Fig. 5b). The lowest 3.7 m of the fault scarp is the most recently exhumed scarp
424 segment and the most intensively sampled. It displays a steep ^{36}Cl concentration gradient,
425 which indicates matching mean and MAP slip rates of 1.0 mm yr^{-1} , for five model
426 earthquakes (Fig. 5c). The highest 2.5 m of the scarp displays a gentler ^{36}Cl concentration
427 gradient relative to the bottom 3.9 m of the scarp as indicated by our drill core samples and
428 the Benedetti et al. (2002) profile. The mean and MAP slip rates for this scarp segment are
429 therefore lower, at 0.8–0.9 mm yr^{-1} (Fig. 5d). Varying the number of earthquakes between
430 three and six has minor influence on the calculated slip rates (Table 2). An increase in mean
431 slip rate occurred between 6.7 and 5.3 kyr (Fig. 5e).

432

433 **4.2 Granulometry of the Sparta fault scarp surface**

434 A first look at the Sparta fault scarp surface yields a misleading impression of homogeneous
435 limestone (Figs. 1, 6a), whereas close inspection of the core samples instead reveals a typical
436 fault breccia (Figs. 6b-d). This breccia consists of angular-to-rounded limestone clasts with

437 axes of 1–7 mm (in the two-dimensional view provided by thin sections) surrounded by
438 matrix/cement in which clasts are <0.1 mm in length. The fault breccia is defined as a
439 protocataclasite, according to the classification of Woodcock and Mort (2008). The
440 composition of the protocataclasite displays large spatial variations, with some portions
441 containing abundant clasts (Fig. 6c), whereas others are dominated by fine matrix (Fig. 6d).
442 The proportion of clasts >2 mm ranges from 5% to 20% vertically along the fault scarp and
443 the proportion of matrix ranges from 5% to 60%. We did not measure the thickness of the
444 protocataclasite but it everywhere exceeds the 3 cm depth of our drill cores.

445

446 **4.3 Sparta fault scarp composition and mineralogy**

447 In addition to a spatially variable granulometry, the fault scarp shows a spatially variable
448 distribution of major and trace elements. The major component is, as expected for limestone,
449 CaO (mean 52.22%) but its concentration varies between 43.83% and 56.64% (Table S3),
450 which exceeds spatial variations in CaO seen elsewhere in limestone normal fault scarps
451 (Carcaillet et al., 2008; Tesson et al., 2016). Quartz (SiO₂) also occurs, and it too displays
452 spatial variations (0.10%–20.82%), with broad peaks occurring at 0.5–0.4 m below the
453 ground, and 0.9–1.2 m, 4.6–4.8 m, and 6.0–6.2 m along the vertical fault scarp profile (Fig. 7;
454 Table S3). An additional peak in SiO₂, but which is not seen in point counting of quartz,
455 occurs at 6.2 m (Fig. 7; Tables S3 and S4). Mean concentrations of other major elements are
456 low in bulk samples, including Al₂O₃ (0.21%), MgO (0.16%), Fe₂O₃ (0.09%), P₂O₅ (0.07%),
457 and K₂O (0.05%; Table S3). However, EDS measurements, such as shown in Figure 8a,
458 reveal that the concentrations of some elements are frequently much higher in intergranular
459 pores (Fig. 8c) than elsewhere in the fault scarp, including Si ≤ 38.3%, Al ≤ 11.7%, Fe ≤
460 48.4%, and K ≤ 7.1% (Table S5). Furthermore, intergranular pores and quartz frequently

461 occur together (Fig. 8b) and the concentration of Al_2O_3 covaries with the much more
462 abundant quartz (SiO_2) (Fig. 7).
463
464 Quartz is revealed by microscopy to be present as randomly oriented rounded-to-angular
465 grains that are $<50\ \mu\text{m}$ in diameter (Figs. 6d, 8b). Quartz is a constituent of the
466 protocataclasite fine matrix that is mostly comprised of microcrystalline calcite precipitates
467 and which cements larger host rock-derived CaCO_3 clasts (Figs. 6b-d, 8b, 9a). Point counting
468 further reveals quartz modes ranging from 0.1% to 15.4% of thin section area (Table S4),
469 with higher abundances correlating to higher abundances of fine matrix. The spatial
470 correlations between SiO_2 , quartz abundances on point counting, and fine matrix are further
471 strengthened by EDS spot elemental analyses (Fig. 9). Here, the two selected spots in the fine
472 matrix display Si abundances of 29.7% and 28.9%, which contrasts with 1.7% and 0.9% for
473 the two spots located on clasts. CaO abundances display an inverse relationship with SiO_2
474 (33.7% and 31.2% for the clasts versus 4.8% and 5.1% for the fine matrix). SiO_2 is present
475 largely as quartz, as evidenced by the strong spatial correlation between quartz and SiO_2
476 along the vertical profile (Fig. 7). Quartz can therefore be used as a proxy for fine matrix
477 abundances in the Sparta fault scarp.

478
479 In addition to the spatial relationship between quartz and fine matrix, we observed in
480 backscatter SEM images that pore spaces, which frequently harbor higher concentrations of
481 Si, Al, K and/or Fe than host rock-derived clasts, are also more abundant in the fine matrix
482 (Fig. 8c). These observations provide evidence that clay particles ($< \mu\text{m}$ -scale) frequently
483 coat pore spaces. The abundance of quartz therefore also provides a proxy for the abundance
484 of clay-coated pore spaces.

485

486 Concentrations of REE-Y vary in a wave-like pattern along the vertical profile, with maxima
487 occurring at -0.4 m, 0.8 m, 2.6 m, 4.0 m, and 6.4 m ($Y = 1.2\text{--}11.1$ ppm; Table S6; Fig. 10).
488 These maxima do not systematically decrease with vertical distance above the hanging wall
489 and are not highest in the soil-mantled portion of the scarp. Yttrium (mean 6.3 ppm), La
490 (mean 5.04 ppm), Nd (mean 3.54 ppm), and Ce (mean 2.31 ppm) have the highest
491 concentrations, whereas all other REE-Y are <1 ppm (Table S6). The concentrations of REE-
492 Y elements co-vary vertically along the scarp surface ($R^2 = 0.95$; Fig. 10a).
493
494 There is no depletion of light (LREE) relative to heavy (HREE) rare-earth elements with
495 increasing height on the subaerially exposed fault scarp, where it ranges between 3.9 and 5.1
496 (Figs. 10b, 11a, Table S6). However, there is a relative depletion of LREE on the scarp
497 surface buried by soil (LREE/HREE is 3.2 to 4.0; Figs. 10b, 11a), with least depletion at 0.40
498 m depth and progressively larger LREE depletion with increasing depth. Peaks and troughs in
499 the LREE/HREE ratio along the vertical profile poorly match peaks and troughs in REE-Y
500 concentrations (Figs. 10a, b), although local minima correspond at 3 m and at 5.2 m on the
501 scarp. Accordingly, the correlation between LREE/HREE and total REE-Y concentration is
502 only weak ($R^2 = 0.36$; Fig. 11b).
503
504 REE-Y concentration maxima occur at locations that correspond closely with the Al_2O_3
505 maxima (Fig. 10a; Table S6). Accordingly, LREE, HREE, and total REE-Y are strongly
506 correlated with Al_2O_3 ($R^2 = 0.92$; Figs. 11c, S3a). Spatial correlations between REE-Y and
507 SiO_2 and K_2O are also observed ($R^2 = 0.56$ and 0.87 , respectively; Fig. S4c, e). Whereas
508 REE-Y concentrations vary in wave-like pattern along the scarp, REE-Y is not enriched, and
509 LREE is depleted relative to HREE, in the soil-covered scarp surface.

510

511 **4.4 Hanging wall soil chemistry and pH**

512 The terra rosa soil mantling the hanging wall primarily comprises aeolian dust (Muhs et al.,
513 2010) and carbonate clasts. At our sample site, the soil thickness at the base of the Sparta
514 fault scarp is 0.8 m and this appears to be stable, at least over the timescale of scarp surface
515 dissolution, as evidenced by a much smoother scarp surface texture below the soil surface
516 compared with the subaerially exposed scarp. Below the organic horizon (~0.1 m thick) the
517 soil is welded, probably by calcite precipitates, and horizons are absent. Soil pH is, in
518 general, slightly acidic along the excavated vertical profile, remaining within a 6.2 to 7.0
519 range (Fig. 12a; Table S7). An outlier occurs at -0.30 m, where the pH is 5.6 ± 0.2 . Soil
520 composition varies with depth (Fig. 12b; Table S8). Concentrations of Si, Al, and K are lower
521 in the organic horizon (11%, 0–5%, and 0.4%, respectively) compared with the remainder of
522 the profile (18%–30%, 5–10%, and 0.5–0.9%, respectively), whereas the concentrations of
523 LE, which includes C, are, as expected, higher in the organic horizon (75%–80%) than in the
524 lower profile segment (51%–64%). The concentration of yttrium ranges from a maximum of
525 36–39 ppm at 0.5–0.6 m depth to a minimum of 11 ppm at 0.1 m depth and its vertical
526 distribution correlates positively with Si ($R^2 = 0.71$), Al ($R^2 = 0.45$), and K ($R^2 = 0.54$), and
527 negatively with pH ($R^2 = -0.52$; Figs. 12c, S4b,d,f; Table S8).

528

529 **5 Discussion**

530 **5.1 Slip rate on the Sparta Fault at Anogia**

531 Average exhumation of the entire scarp up to the present day is 0.7–0.8 mm yr⁻¹ (Fig. 5a;
532 Table 2). This compares with an exhumation rate of 1.1–1.2 mm yr⁻¹ up to the 464 B.C.E.
533 earthquake (if an earthquake occurred now, the rate up to the present day would increase).
534 Our data show an increase in average slip rate during exhumation of the scarp from an initial
535 0.8–0.9 mm yr⁻¹ between 6.5 and 7.7 kyr ago to 1.0 mm yr⁻¹ between 3.0 and 6.0 kyr ago

536 (Fig. 5e). These slip rates directly reflect the steeper ^{36}Cl gradient for the lower 4.0 m of the
537 fault scarp compared with the gentler gradient from 4.0 to 6.5 m (Figs. 2 and 3c). Although
538 the sampling density is highest over the lowermost 4 m, we have confidence in the lower
539 inferred average slip rate for the higher, older part of the scarp because both our dispersed
540 drill core samples and the Benedetti et al. (2002) profile indicate a lower ^{36}Cl concentration
541 gradient (in trend, rather than absolute values) above 4 m. The MAP model (Fig. 3a) indicates
542 that three scarp exhuming earthquakes may have occurred during 5000-6000 years ago (MAP
543 average slip rate 1.1 mm yr^{-1}), which is consistent with an increase in average slip rate during
544 this period observed in the slip rate versus time plot (Fig. 5e). The lower rate of exhumation
545 for the upper ~ 2.5 m reflects an apparent quiescent period prior to these earthquakes. MCMC
546 modelling does not indicate that earthquakes have contributed to exhumation of the Sparta
547 fault more recently than the last historically recorded event at 464 B.C.E. Periods of
548 quiescence appear to characterize normal faults in the Mediterranean region (Cowie et al.,
549 2017; Goodall et al., 2021) and so the recent 2.5 kyr period of quiescence is not necessarily
550 indicative that another earthquake is imminent.

551

552 Our data do not uniquely specify the number and timing of scarp exhumation events and we
553 have been unable to identify other faults along the eastern flank of the Taygetos Mountains
554 suitable for ^{36}Cl analyses that with the Sparta fault may form part of a system, across which
555 slip is distributed. We therefore limit our interpretations to averaged slip rates and the timing
556 of changes in these rates for the Sparta fault at Anogia, rather than attempting to identify
557 individual earthquakes or draw conclusions on regional fault kinematics and associated
558 seismic hazards.

559

560 **5.2 Methodological and geological sources of uncertainty in the ^{36}Cl data**

561 A feature of the ^{36}Cl data is that our Anogia A and B profiles display systematically lower
562 concentrations than the Benedetti et al. (2002) profile (Fig. 2). The Benedetti et al. (2002)
563 profile also displays variations between adjacent sample points that exceed those observed in
564 our profiles. We interpret the systematic differences in ^{36}Cl concentration between our
565 profiles and the Benedetti et al. (2002) profile as reflecting methodological differences
566 related to advances in sample preparation chemistry at PRIME-Lab, Purdue University. For
567 this reason, we elect not to model the Benedetti et al. (2002) data using the MCMC
568 methodology.

569
570 Whereas our Anogia A and B profiles display corresponding trends with increasing elevation
571 on the fault scarp, Anogia B samples have generally lower ^{36}Cl concentrations (Fig. 2).
572 Indeed, six of its 19 ^{36}Cl concentrations do not overlap within uncertainty with concentrations
573 of corresponding samples on the 3.9 m Anogia A profile, including four points located
574 between 1.0 m and 1.3 m. We interpret these differences as indicating that the fault scarp at
575 Anogia B has been either partly shielded from cosmogenic radiation, has eroded more than
576 the scarp surface at Anogia A, or contains a higher concentration of non-calcite impurities. Of
577 potential additional relevance is that the texture of the scarp surface at Anogia B is smoother
578 than at the location of Anogia A. Because a similarly smooth texture also characterizes the
579 scarp surface presently buried by colluvium mantling the hanging wall, the smooth texture at
580 the location of Anogia B may indicate either recent burial of the scarp surface by colluvium
581 and/or CaCO_3 dissolution/precipitation occurring at a higher rate than at locations where
582 the exposed scarp surface texture is rougher. If a smooth texture reflects erosion through
583 CaCO_3 dissolution, there might be preferential flow, or seepage, of water from the hillslope
584 above the scarp at the location of Anogia B. Observed lumps of colluvium cemented to the
585 Sparta fault scarp, at locations perched above the present hanging wall surface (Fig. S1)
586 partially shield the underlying scarp surface today. However, had this previously occurred at

587 the location of Anogia B, an eroded colluvial lump would be evidenced in the hanging wall
588 sediments. On the contrary, there is no colluvial lump, but rather a sub-horizontal surface is
589 present with an expression that differs little from the surface below the Anogia A profile. The
590 inter-profile differences in ^{36}Cl concentrations illustrate the value in taking samples for ^{36}Cl
591 measurements from more than one vertical profile at a particular location, because ^{36}Cl
592 concentrations can vary either through spatial variations in non-calcite impurities or past
593 shielding by sediments or bedrock, which can otherwise be difficult to detect. Partial
594 shielding may impact the interpretation of paleoseismicity, including the timing, number and
595 magnitudes of earthquakes, through locally lowered ^{36}Cl concentrations.

596

597 **5.3 The effects of mineralogical impurities on ^{36}Cl concentrations**

598 Mineralogical impurities embedded in the fault breccia that comprise the scarp surface appear
599 to be a key geological reason for spatial variations in the concentration of ^{36}Cl . Measurements
600 of chemistry and mineralogy at Anogia B indicate that SiO_2 comprises 0.1–20.8 wt.% of the
601 scarp. Because the concentration of CaCO_3 is inversely correlated with SiO_2 (largely quartz),
602 then peaks in SiO_2 might coincide with troughs in ^{36}Cl , although a simple relationship
603 vertically along the scarp is obscured by the relationship between ^{36}Cl concentration and
604 exposure duration. A local peak in SiO_2 of 12–15 wt.% coincides with a local low in ^{36}Cl
605 concentration at Anogia B between about 0.6 and 1.2 m on the scarp (Figs. 2 and 7, Tables S1
606 and S3). A distinct low in ^{36}Cl concentration at 1.6 m also corresponds with a local peak in
607 SiO_2 of 9 wt.%. However, the magnitudes of the variations are inconsistent between these
608 two locations, such that a high peak in SiO_2 corresponds with a small reduction of ^{36}Cl at
609 0.6–1.2 m and vice versa at 1.6 m. Because ^{36}Cl is also produced by spallation on K ($162 \pm$
610 $24 \text{ atoms g}^{-1} \text{ yr}^{-1}$ at SLHL; Evans et al., 1997), Fe ($1.3 \pm 0.1 \text{ atoms g}^{-1} \text{ yr}^{-1}$ – $1.9 \pm 0.2 \text{ atoms g}^{-1}$
611 yr^{-1} at SLHL; Stone, 2005; Moore and Granger, 2019), and Ti ($13 \pm 3 \text{ atoms g}^{-1} \text{ yr}^{-1}$ at

612 SLHL; Fink et al., 2000), noise in the ^{36}Cl data might also partly reflect the relative
613 abundances of these elements. However, this appears to be insignificant given that measured
614 concentrations of these elements are extremely low (concentrations of K_2O , Fe_2O_3 , and TiO_2
615 are 0–0.12%, 0.03–0.24%, and 0–0.02%, respectively; Fig. S4, Table S3). Other elements,
616 seemingly present as trace amounts of clay, lining pores in the fault breccia (Fig. 7, Table
617 S3), are also an insignificant contributor to variations in ^{36}Cl concentrations. For the Sparta
618 fault at Anogia, quartz embedded in the fault breccia may be the key mineralogical impurity
619 that is likely contributing variance to the ^{36}Cl concentrations, which in turn impacts our
620 ability to obtain unequivocal dates of individual earthquakes.

621

622 **5.4 Interpretation of REE-Y distributions and implications for paleoseismicity**

623 REE-Y cannot be used to infer imprints of former soil profiles on the Sparta fault at Anogia.
624 Petrographic analyses indicate that the Sparta fault scarp is composed of a protocataclasite
625 consisting of calcite clasts derived from the host limestone, microcrystalline calcite cement,
626 and quartz (Figs. 6, 7). Furthermore, EDS analysis indicates that trace amounts of clay, such
627 as illite, are lining pores where microcrystalline calcite cement and quartz are located (Fig. 8;
628 Carcaillet et al., 2008). We infer that REE-Y are adsorbed onto clay minerals lining pores in
629 the fine-grained matrix of the fault breccia, as indicated by correlations between REE-Y and
630 each of Al, K, Si, and Fe ($R^2 = 0.92, 0.87, 0.56, \text{ and } 0.47$, respectively; Fig. S4a-c) and
631 between Y and both Si and Al in the hanging wall colluvium ($R^2 = 0.71 \text{ and } 0.45$,
632 respectively; Figs. 12c and S4b,c). Supplementary data from the Kaparelli fault ($R^2 = 0.95$ for
633 Si; Figs. 1a and S5a) and Magnola fault hanging walls ($R^2 = 0.98$ for both Si and Al; Fig.
634 S5b,c and electronic appendix to Manighetti et al., 2010) also indicate REE-Y may be
635 adsorbed to clay embedded in limestone fault scarps. These correlations generally contrast
636 with a weaker negative correlation between Y and pH ($R^2 = 0.52$) for the hanging wall soil on

637 the Sparta Fault (Fig. 12c). Soil pH does not appear to be the dominant control on REE-Y
638 distributions in the Sparta fault scarp, which differs to interpretations on other limestone fault
639 scarps (Carcaillet et al., 2008; Bello et al., 2023).

640

641 We propose a causative relationship between the vertical distributions of REE-Y and clay on
642 the Sparta fault scarp. This reasoning is supported by the following observations:

643 (i) The Sparta fault scarp REE-Y concentrations are equivalent to (Nuriel et al., 2012;
644 Goodfellow et al., 2017) or higher than those measured elsewhere in platform
645 limestone (Carcaillet et al., 2008; Mouslopoulou et al., 2011), but Y
646 concentrations are lower in the adjacent hanging wall soil (REE were not
647 measured in the soil; Tables S6, S8).

648 (ii) If REE-Y exchange between the soil and fault scarp occurs according to the
649 Carcaillet et al. (2008) model, fractionation of LREE and HREE elements is
650 expected. For example, LREE might be preferentially mobilized (Takahashi et al.,
651 2005; Carcaillet et al., 2008), leading to an enrichment of LREE relative to HREE
652 in the fault scarp, where there are peaks in total REE-Y. Conversely, LREE may
653 be depleted relative to HREE where there are troughs in total REE-Y. However,
654 the proportion of LREE to HREE remains confined to a constant range vertically
655 along the subaerial section of Sparta fault scarp (Figs.10b, 11a), is weakly
656 correlated with total REE-Y ($R^2 = 0.36$; Fig. 11b), and is relatively depleted at all
657 measured depths beneath the soil surface (Fig. 10b).

658 (iii) There is no systematic decrease with distance above the hanging wall in total
659 REE-Y (Fig. 10a, b), in contrast to declining concentrations with distance above
660 the hanging wall on the Magnola fault (Carcaillet et al., 2008).

661 Adsorption of REE-Y onto clay has been observed in regolith (Borst et al., 2020) but has not
662 been previously discussed in the context of interpreting paleoseismicity on limestone fault
663 scarps.

664

665 Although we infer that adsorption of REE-Y onto clay minerals embedded in fault breccia
666 dominates on the Sparta fault, the approximate coincidence of the subsurface peak in scarp
667 LREE/HREE and total REE-Y with the mid-profile peak in soil pH (Figs. 10, 12a, b)
668 provides evidence of REE-Y exchange between the scarp and the soil. However, the
669 consequence is LREE depletion in the scarp, rather than enrichment (Fig. 10b), and it is
670 unclear why this apparent depletion is not replicated on the subaerially exposed scarp. One
671 possibility is that colluvium accumulation postdates the most recent earthquake although, if
672 so, low ^{36}Cl concentrations in the buried scarp surface indicate that the soil accumulation was
673 co-seismic with the last earthquake or accumulated soon afterwards. It is also unclear why
674 colluvium would accumulate only after the most recent earthquake. An alternative possibility
675 is that a superficial LREE-depleted zone has been eroded from the subaerial scarp surface
676 through dissolution. This would imply erosion of centimeters of scarp surface since the last
677 known earthquake on the Sparta fault at 464 B.C.E. (an erosion rate of 0.01 mm yr^{-1} over the
678 past 2500 years would remove 2.5 cm of scarp surface). Yet another possibility is that
679 perhaps more time is required to increase LREE to concentrations seen on the subaerial scarp
680 surface, but 2500 years have already passed since the most recent known earthquake and
681 maximum REE-Y enrichment has been inferred to occur within 500 years on the Spilli and
682 Magnola faults (Manighetti et al., 2010; Mouslopoulou et al., 2011). Alternatively, LREE
683 enrichment occurs after scarp exhumation, perhaps through exchange with aeolian dust
684 fallout, as has been observed in Dead Sea halite (Censi et al., 2023). Such dust inputs may
685 supply REE-Y (Yang et al., 2007), as indicated by the correlation between Y and Si in the

686 hanging wall colluvium (Fig. 12b, c), contribute fine-grained mineral soil to the hanging wall
687 colluvium, and may lower soil pH through buffering locally-sourced CaCO_3 . However, given
688 that inputs of Saharan dust are ubiquitous throughout the Mediterranean (Stuut et al., 2009)
689 and can comprise a large component of soils in the region (Muhs et al., 2010; Styllas et al.,
690 2023), similar patterns of LREE depletion in the soil-covered scarp surface relative to the
691 subaerial scarp surface are expected to have been observed elsewhere, which is not the case
692 (Carcaillet et al., 2008; Manighetti et al., 2010; Mouslopoulou et al., 2011; Tesson et al.,
693 2016; Bello et al., 2023).

694

695 For the Sparta fault scarp, the presence of clay likely relates to fault breccia formation at
696 considerable depths beneath the Earth's surface, rather than subaerial weathering processes.
697 The formation of protocataclasite occurs beneath the Earth's surface at depths that may range
698 from meters to up to thousands of meters. A model for this involves fluids moving along the
699 Sparta fault, primarily associated with seismic events. These fluids dissolve CaCO_3 from the
700 host-limestones and potentially also silicate minerals from psammitic and pelitic
701 (meta)sediments, where they are dissected by the fault. In association with variations in
702 temperature and pressure along the fault, chemical saturation of these fluids results in
703 precipitation of clay, quartz, and microcrystalline calcite, which cements clasts of host-rock
704 derived limestone into the fault breccia. Subsequent faulting re-fractures the breccia and
705 particle comminution over time produces quartz grains that are rounded-to-angular in shape,
706 randomly oriented, and $<50 \mu\text{m}$ (Figs. 6, 8). The fault breccia may also have undergone
707 multiple generations of microcrystalline calcite re-cementing from re-circulating fluids. As an
708 alternative to a dissolution-precipitation model, clay and quartz emplacement may involve
709 fluid entrainment of particles and grains from clay- and quartz-bearing sedimentary units
710 during faulting, as has been observed elsewhere (e.g., Darwin, 1840; Roy, 1946; Brandon,

711 1972; Röshoff and Cosgrove, 2002). This process may also be accompanied by comminution
712 of fault-zone quartz grains derived from psammitic rocks. We tentatively exclude a
713 contemporary aeolian source for the clay and quartz because there is no documented
714 mechanism to transport clay particles and quartz grains from the soil to centimeters into a
715 fault scarp. We cannot distinguish soil to scarp clay and quartz migrations on the Sparta fault
716 which has been observed, for example, at the micrometer scale in surface coatings on the
717 Magnola fault, because that scarp is comprised of pure carbonate (Carcaillet et al., 2008). It is
718 likely that limestone fault scarps are generally composed of fault breccias (Agosta and Aydin,
719 2006; Carcaillet et al., 2008; Nuriel et al., 2012) and that where a fault intersects varying
720 lithologies, chemical and mineralogical heterogeneities may occur in the fault breccia, as
721 observed on the Sparta fault. Where they occur, these heterogeneities may control the spatial
722 distribution of REE-Y, independent of any spatial reorganization of REE-Y attributable to
723 subaerial weathering. If, as we infer, the spatial patterning of REE-Y, quartz, and clay is
724 inherited from depth, the observed wave-like signal (Figs. 7, 10) may reflect sorting and
725 cementing of breccia around surface asperities on the fault plane. The resulting infilling of
726 depressions with fault gouge may create a successively more polished and localized fault
727 plane along which friction is lowered, thereby permitting larger slip (i.e., larger earthquakes)
728 along the fault (Sagy and Brodsky, 2009). Whereas REE-Y concentrations do not appear to
729 be a reliable indicator of Holocene paleoseismicity of the Sparta fault, they may instead
730 reveal processes that localize slip to a discrete fault plane.

731

732 Whereas the Sparta Fault displays concentrations of clay and quartz impurities that are much
733 higher than on other reported limestone fault scarps, three general implications emerge for
734 using REE-Y in making inferences of paleoseismicity. Firstly, the potential control on REE-
735 Y distributions of even trace amounts of non-calcite impurities in the breccia comprising fault

736 scarps should be considered through analyses of thin sections in addition to scarp chemistry.
737 Secondly, soil acidity and REE-Y enrichment, including any resulting exchange with the
738 buried scarp, may peak some tens of centimeters below the colluvium surface. Peaks in REE-
739 Y concentrations on subaerial fault scarp surfaces may not therefore reflect former soil
740 surfaces, even if there is soil-scarp exchange of REE-Y. In addition, the Sparta fault scarp
741 REE-Y data indicate that it may be rewarding to focus on up-scarp variations in LREE/HREE
742 ratios rather than on REE-Y concentrations, because these may be a sensitive indicator of
743 REE-Y exchange processes occurring beneath soil covers (Fig 10b). Lastly, relationships
744 between REE-Y distributions and soil mineralogy should be more closely assessed, in
745 addition to the commonly modelled and studied effects of pH (e.g., Carcaillet et al., 2008;
746 Manighetti et al., 2010; Mouslopoulou et al., 2011; Moraetis et al., 2015, 2023; Tesson et al.,
747 2016; Bello et al., 2023). Fine grained mineral inputs through aeolian dust fallout comprise
748 substantial volumes of Mediterranean soils (Muhs et al., 2010; Styllas et al., 2023) and
749 decadal to millennial variations in dust fluxes may directly impact on REE-Y distributions in
750 hanging wall soils and potentially in scarp surfaces, in locations where soil-scarp REE-Y
751 exchange is important. These fluctuations may contribute to REE-Y patterns in soils that are
752 difficult to predict and in scarp surfaces reflect (climatic and pedogenic) processes that may
753 complicate potential paleoseismic inferences.
754
755 Moraetis et al. (2023) consider REE-Y analyses an established method in paleoseismicity.
756 Our detailed study errs towards caution; there remain important uncertainties regarding
757 processes of REE-Y enrichment and depletion in limestone fault scarps. Indeed, we maintain
758 that there is considerable uncertainty regarding how the resulting patterns should be
759 interpreted with respect to paleoseismicity. Fundamentally, it remains unclear how far into
760 buried scarp surfaces the REE-Y can be adsorbed from soil or incorporated into calcite

761 through dissolution-precipitation. A dissolution rate of 0.001 mm yr^{-1} will erode 1 cm from a
762 subaerially exposed scarp surface over 10 000 years, which is about the timescale considered
763 to be relevant to assessing full seismic cycles and therefore making accurate assessments of
764 paleoseismicity (Mouslopoulou et al., 2012; Tesson et al., 2016). Even such a slow rate of
765 subaerial scarp dissolution will therefore remove any REE-Y signals inherited from former
766 soil cover unless that exchange extends to centimeters into the scarp.

767

768 **6 Conclusion**

769 Modelling of ^{36}Cl data from the Sparta fault at Anogia, Greece, indicates an increase in
770 average slip rate during exhumation of the scarp from $0.8\text{--}0.9 \text{ mm yr}^{-1}$ between 7.7 and 6.5
771 kyr ago to 1.0 mm yr^{-1} between 6.5 and 2.5 kyr ago (the timing of the historic 464 B.C.E.
772 earthquake). Average exhumation of the entire scarp is $0.7\text{--}0.8 \text{ mm yr}^{-1}$. Modelling does not
773 indicate that earthquakes may have contributed to exhumation of the Sparta fault since 464
774 B.C.E.

775

776 The Sparta fault scarp is impure; it is composed of fault breccia, which contains quartz and
777 clay-lined pores in addition to calcite. The vertical distribution of REE-Y is highly correlated
778 with the pore-clay and may indicate processes that localize slip to a discrete fault plane deep
779 below the ground surface. The potential exchange of REE-Y between the hanging wall
780 colluvium and the adjacent footwall scarp is overwhelmed at this site by REE-Y attached to
781 the pore clays inherited from depth. Because of this, Holocene earthquakes and their slip
782 distances and magnitudes cannot be inferred for the Sparta fault from REE-Y concentrations.
783 Whereas this is probably true also for similar impure limestone fault scarps elsewhere, other
784 controls on REE-Y distributions, in addition to hanging wall soil pH, should be evaluated in

785 attempting paleoseismic inferences more generally from normal fault scarps developed in
786 limestone.

787

788 **Author contribution**

789 AS and APS conceived the study and acquired the funding for RF. BWG, APS, and AS
790 supervised RF. APS, AS, BWG, MWC, and RF participated in fieldwork. RF conducted the
791 analysis of scarp composition and made initial interpretations. BWG performed additional
792 analyses and earthquake modelling, and wrote the manuscript. GC led the laboratory
793 preparation of samples for ^{36}Cl measurement, together with BWG, and calculated ^{36}Cl
794 concentrations from the AMS data. All authors contributed to data interpretation and
795 manuscript editing.

796

797 **Competing interests**

798 Arjen P. Stroeven is a member of the editorial board for *Solid Earth*.

799

800 **Acknowledgements**

801 We thank Mikael Amlert for his assistance with field safety and sampling, Giorgos Maneas,
802 station manager of the Navarino Environmental Observatory (NEO), for his extensive
803 assistance with field logistics, and our deceased friend, Dan Zetterberg, Department of
804 Geological Sciences, Stockholm University, for his assistance with thin section preparations.
805 This project was funded by the Stockholm University Research School for teachers focusing
806 on Natural Hazards financed by the Swedish Research Council and by a grant from NEO. We
807 gratefully acknowledge funding for fieldwork from the Swedish Society for Anthropology
808 and Geography Andréé Fund to Fritzon.

809

810 **References**

- 811 Agosta, F. and Aydin, A.: Architecture and deformation mechanism of a basin bounding
812 normal fault in Mesozoic platform carbonates, central Italy. *Journal of Structural*
813 *Geology*, 28, 1445–1467, 2006.
- 814 Armijo, R., Lyon-Caen, H., and Papanastassiou, D.: A possible normal-fault rupture for the
815 464 BC Sparta earthquake. *Nature*, 351, 137–139, 1991.
- 816 Bello, S., Perna, M.G., Consalvo, A., Brozzetti, F., Galli, P., Cirillo, D., Andrenacci, C.,
817 Tangari, A.C., Carducci, A., Menichetti, M., Lavecchia, G., Stoppa, F., and Rosatelli, G.:
818 Coupling rare earth element analyses and high-resolution topography along fault scarps to
819 investigate past earthquakes: A case study from the Southern Apennines (Italy).
820 *Geosphere*, 19, 1348–1371, 2023.
- 821 Benedetti, L., Finkel, R., Papanastassiou, D., King, G., Armijo, R., Ryerson, F., Farber, D.,
822 and Flerit, F.: Post-glacial slip history of the Sparta fault (Greece) determined by ^{36}Cl
823 cosmogenic dating: Evidence for non-periodic earthquakes. *Geophysical Research*
824 *Letters*, 29, 1246, 2002.
- 825 Benedetti, L., Manighetti, I., Gaudemer, Y., Finkel, R., Malavieille, J., Pou, K., Arnold, M.,
826 Aumaître, G., Bourlès, D. and Keddadouche, K.: Earthquake synchrony and clustering on
827 Fucino faults (Central Italy) as revealed from in situ ^{36}Cl exposure dating. *Journal of*
828 *Geophysical Research, Solid Earth*, 118, 4948–4974, 2013.
- 829 Borst, A. M., Smith, M. P., Finch, A. A., Estrade, G., Villanova-de-Benavent, C., Nason, P.,
830 Marquis, E., Horsburgh, N. J., Goodenough, K. M., Xu, C., Kynický, J. and Geraki,

831 K.: Adsorption of rare earth elements in regolith-hosted clay deposits. *Nature*
832 *Communications*, 11, 4386, 2020.

833 Brandon, A.: Clastic dykes in the Namurian shales of County Leitrim, Republic of Ireland.
834 *Geological Magazine*, 109, 361–367, 1972.

835 Bubeck, A., Wilkinson, M., Roberts, G. P., Cowie, P. A., McCaffrey, K. J. W., Phillips, R.
836 and Sammonds, P.: The tectonic geomorphology of bedrock scarps on active normal
837 faults in the Italian Apennines mapped using combined ground penetrating radar and
838 terrestrial laser scanning. *Geomorphology*, 237, 38–51, 2015.

839 Carcaillet, J., Manighetti, I., Chauvel, C., Schlagenhauf, A., and Nicole, J.-M.: Identifying
840 past earthquakes on an active normal fault (Magnola, Italy) from the chemical analysis of
841 its exhumed carbonate fault plane. *Earth and Planetary Science Letters*, 271, 145–158,
842 2008.

843 Censi, P., Sirota, I., Zuddas, P., Lensky, N.G., Crouvi, O., Cangemi, M. and Piazzese, D.:
844 Rare earths release from dissolving atmospheric dust and their accumulation into
845 crystallising halite: The Dead Sea example. *Science of the Total Environment*, 875,
846 162682, 2023.

847 Cowie, P.A., Phillips, R.J., Roberts, G.P., McCaffrey, K., Zijerveld, L.J.J., Gregory, L.C.,
848 Faure Walker, J., Wedmore, L.N.J., Dunai, T.J., Binnie, S.A., Freeman, S.P.T.H.,
849 Wilcken, K., Shanks, R.P., Huisman, R.S., Papanikolaou, I., Michetti, A.M. and
850 Wilkinson, M.: Orogen-scale uplift in the central Italian Apennines drives episodic
851 behaviour of earthquake faults. *Scientific Reports*, 7, 44858, 2017.

852 Darwin, C: Geological observations in the volcanic islands and parts of South America
853 visited during the voyage of H.M.S. Beagle. London, 1840.

854 Dawood, R., Matmon, A., Benedetti, L., ASTER Team and Siman-Tov, S.: Multi-segment
855 earthquake clustering as inferred from ³⁶Cl exposure dating, the Bet Kerem fault system,
856 northern Israel. *Tectonics*, 43, e2023TC007953, 2024.

857 Dramis, F, and Blumetti, A.M.: Some considerations concerning seismic geomorphology and
858 paleoseismology. *Tectonophysics*, 408, 177–191, 2005.

859 Evans, J.M, Stone, J.O.H., Fifield, L.K., and Cresswell, R.G.: Cosmogenic chlorine-36
860 production in K-feldspar. *Nuclear Instruments and Methods in Physics Research B*, 123,
861 334–340, 1997.

862 Fink, D., Vogt, S., and Hotchkis, M.: Cross-sections for ³⁶Cl from Ti at E_p = 35–150 MeV:
863 Applications to in-situ exposure dating. *Nuclear Instruments and Methods in Physics*
864 *Research B*, 172, 861–866, 2000.

865 Friedrich, A. M., Wernicke, B. P., Niemi, N. A., Bennett, R.A. and Davis, J.L.: Comparison
866 of geodetic and geologic data from the Wasatch region, Utah, and implications for the
867 spectral character of Earth deformation at periods of 10 to 10 million years, *Journal of*
868 *Geophysical Research: Solid Earth*, 108, 2199, 2003.

869 Godey, S., Bossu, R., and Guilbert, J.: Improving the Mediterranean seismicity picture thanks
870 to international collaborations. *Physics and Chemistry of the Earth, Parts A/B/C*, 63, 3–
871 11, 2013.

872 Goodall, H. J., Gregory, L. C., Wedmore, L. N. J., McCaffrey, K. J. W., Amey, R. M. J.,
873 Roberts, G. P., Shanks, R.P., Phillips, R.J. and Hooper, A. Determining histories of slip
874 on normal faults with bedrock scarps using cosmogenic nuclide exposure data. *Tectonics*,
875 40, e2020TC006457, 2021.

876 Goodfellow, B.W., Viola, G., Bingen, B., Nuriel, P. and Kylander-Clark, A.: Paleocene
877 faulting in SE Sweden from U-Pb dating of slickenfiber calcite. *Terra Nova*, 29, 321–328,
878 2017.

879 Gürpinar, A.: The importance of paleoseismology in seismic hazard studies for critical
880 facilities. *Tectonophysics*, 408, 23–28, 2005.

881 Hastings, W.K.: Monte Carlo sampling methods using Markov chains and their applications.
882 *Biometrika*, 57, 97–109, 1970.

883 Hickson, C.J. and Juras, S.J.: Sample contamination by grinding. *Canadian Mineralogist*, 24,
884 585–589, 1986.

885 Hutchison, C.S.: *Laboratory Handbook of Petrographic Techniques*. Wiley-Interscience, New
886 York, 527 pp, 1974.

887 Iezzi, F., Roberts, G., Faure Walker, J., Papanikolaou, I., Ganas, A., Deligiannakis, G., Beck,
888 J., Wolfers, S. and Gheorghiu, D.: Temporal and spatial earthquake clustering revealed
889 through comparison of millennial strain-rates from ³⁶Cl cosmogenic exposure dating and
890 decadal GPS strain-rate. *Scientific Reports*, 11, 23320, 2021.

891 Institute for Geology and Subsurface Research: Sparti Sheet, photogeological map of Greece,
892 1969.

893 Jolivet, L., Faccenna, C., Huet, B., Labrousse, L., Le Pourhiet, L., Lacombe, O., Lecomte, E.,
894 Burov, E., Denèle, Y., Brun, J.-P., Philippon, M., Paul, A., Salaün, G., Karabulut, H.,
895 Piromallo, C., Monié, P., Gueydan, F., Okay, A.I., Oberhänsli, R., Pourteau, A., Augier,
896 R., Gadenne, L. and Driussi, O.: Aegean tectonics: Strain localisation, slab tearing and
897 trench retreat. *Tectonophysics*, 597–598, 1–33, 2013.

898 Lifton, N.A., Bieber, J.W., Clem, J.M., Duldig, M.L., Evenson, P., Humble, J.E. and Pyle, R.:
899 Addressing solar modulation and long-term uncertainties in scaling secondary cosmic
900 rays for in situ cosmogenic nuclide applications. *Earth and Planetary Science Letters*,
901 239, 140–161, 2005.

902 Lifton, N.A., Sato, T. and Dunai, T.J.: Scaling in situ cosmogenic nuclide production rates
903 using analytical approximations to atmospheric cosmic-ray fluxes. *Earth and Planetary
904 Science Letters*, 386, 149–160, 2014.

905 Lifton, N.A., Smart, D.F. and Shea, M.A.: Scaling time-integrated in situ cosmogenic nuclide
906 production rates using a continuous geomagnetic model. *Earth and Planetary Science
907 Letters*, 268, 190–201, 2008.

908 Manighetti, I., Boucher, E., Chauvel, C., Schlagenhauf, A. and Benedetti, L.: Rare earth
909 elements record past earthquakes on exhumed limestone fault planes. *Terra Nova*, 22,
910 477–482, 2010.

911 Marrero, S.M., Phillips, F.M., Caffee, M.W. and Gosse, J.C.: CRONUS-Earth cosmogenic
912 ³⁶Cl calibration. *Quaternary Geochronology*, 31, 199–219, 2016.

913 McCalpin, J.P.: *Paleoseismology*, Academic press, 613 pp., 2009.

914 McDonough, W.F. and Sun, S.-s.: The composition of the Earth. *Chemical Geology*, 120,
915 223–253, 1995.

916 Metropolis, N., Rosenbluth, A. W., Rosenbluth, M. N., Teller A. H. and Teller, E.: Equation of state
917 calculations by fast computing machines. *Journal of Chemical Physics*, 21, 1087–1092, 1953.

918 Michetti, A.M., Audemard, F.A. and Marco, S.: Future trends in paleoseismology: Integrated
919 study of the seismic landscape as a vital tool in seismic hazard analyses *Tectonophysics*,
920 408, 3–21, 2005.

921 Mitchell, S.G., Matmon, A., Bierman, P.R., Enzel, Y., Caffee, M. and Rizzo, D.:
922 Displacement history of a limestone normal fault scarp, northern Israel, from cosmogenic
923 ³⁶Cl. *Journal of Geophysical Research: Solid Earth*, 106, 4247–4264, 2001.

924 Moore, A. K. and Granger, D. E.: Calibration of the production rate of cosmogenic ³⁶Cl from
925 Fe. *Quaternary Geochronology*, 51, 87–98, 2019.

926

927 Moraetis, D., Mouslopoulou, V., Pratikakis, A., Begg J. and Pracejus, B.: The mechanism of
928 REE-Y impregnation on active carbonate normal fault scarps. *Applied Geochemistry*,
929 155, 105703, 2023.

930 Mouslopoulou, V., Moraetis, D. and Fassoulas, C.: Identifying past earthquakes on carbonate
931 faults: Advances and limitations of the ‘Rare Earth Element’ method based on analysis of
932 the Spili Fault, Crete, Greece. *Earth and Planetary Science Letters*, 309, 45–55, 2011.

933 Mouslopoulou, V., Nicol, A., Walsh, J.J., Begg, J.G., Townsend, D.B. and Hristopoulos, D.T.:
934 Fault-slip accumulation in an active rift over thousands to millions of years and the
935 importance of paleoearthquake sampling, *Journal of Structural Geology*, 36, 71–80, 2012.

936 Mozafari, N., Özkaymak, C., Sümer, Ö, Tikhomirov, D., Uzel, B., Yeşilyurt, S., Ivy-Ochs, S.,
937 Vockenhuber, C., Sözbilir, H. and Akçar, N.: Seismic history of western Anatolia during
938 the last 16 kyr determined by cosmogenic ³⁶Cl dating. *Swiss Journal of Geosciences*, 115,
939 5, 2022.

940 Muhs, D.R., Budahn, J., Avila, A., Skipp, G., Freeman, J. and Patterson, D.: The role of
941 African dust in the formation of Quaternary soils on Mallorca, Spain and implications for
942 the genesis of Red Mediterranean soils. *Quaternary Science Reviews*, 29, 2518–2543,
943 2010.

944 Muzikar, P., Elmore, D. and Granger, D.E.: Accelerator mass spectrometry in geologic
945 research. *Geological Society of America Bulletin*, 115, 643–654, 2003.

946 Nuriel, P., Rosenbaum, G., Zhao, J.-X., Feng, Y., Golding, S.D., Villemant, B. and
947 Weinberger, R.: U-Th dating of striated fault planes. *Geology*, 40, 647–650, 2012.

948 Palumbo, L., Benedetti, L., Bourlès, D., Cinque, A. and Finkel, R.: Slip history of the
949 Magnola fault (Apennines, Central Italy) from ³⁶Cl surface exposure dating: evidence for
950 strong earthquakes over the Holocene. *Earth and Planetary Science Letters*, 225, 163–
951 176, 2004.

952 Papanikolaou, I.D., Roberts, G.P., Deligiannakis, G., Sakellariou, A. and Vassilakis, E.: The
953 Sparta Fault, Southern Greece: From segmentation and tectonic geomorphology to
954 seismic hazard mapping and time dependent probabilities. *Tectonophysics*, 597–598, 85–
955 105, 2013.

956 Pope, R.J. and Wilkinson, K.N.: Reconciling the roles of climate and tectonics in Late
957 Quaternary fan development on the Spartan piedmont, Greece. In: A.M. Harvey, A.E.
958 Mather, and M. Stokes, (Eds), *Alluvial Fans: Geomorphology, Sedimentology,*
959 *Dynamics*. Geological Society, London, Special Publications, 251, 133–152, 2005.

960 Röshoff, K. and Cosgrove, J.: Sedimentary dykes in the Oskarshamn-Västervik area. A study
961 of the mechanism of formation. *SKB Report R-02-37*, 98 pp, 2002.

962 Roy, C.J.: Clastic dykes of the Pikes Peak region. Abstract. *Geological Society of America*
963 *Bulletin*, 57, 1226, 1946.

964 Sagy, A. and Brodsky, E.E.: Geometric and rheological asperities in an exposed fault zone.
965 *Journal of Geophysical Research*, 114, B02301, 2009.

966 Schlagenhauf, A., Gaudemer, Y., Benedetti, L., Manighetti, I., Palumbo, L.,
967 Schimmelpfennig, I., Finkel, R. and Pou, K.: Using *in situ* Chlorine-36 cosmonuclide to
968 recover past earthquake histories on limestone normal fault scarps: a reappraisal of
969 methodology and interpretations. *Geophysical Journal International*, 182, 36–72, 2010.

970 Sharma, P., Kubik, P.W., Fehn, U., Gove, H.E., Nishiizumi, K. and Elmore, D.: Development
971 of ³⁶Cl Standards for AMS. *Nuclear Instruments & Methods in Physics Research Section*
972 *B-Beam Interactions with Materials and Atoms*, 52, 410–415, 1990.

973 Sikora, F.J. and Moore, K.P. (Eds.): *Soil Test Methods from the Southeastern United States*.
974 *Southern Cooperative Series Bulletin*, 419, 211 p., 2014.

975 Stone, J.O.: Air pressure and cosmogenic isotope production. *Journal of Geophysical*
976 *Research: Solid Earth*, 105, 23753–23759, 2000.

- 977 Stone, J.O.: Terrestrial chlorine-36 production from spallation of iron. In: Abstract of 10th
978 International Conference on Accelerator Mass Spectrometry, Berkeley, California, USA.,
979 2005.
- 980 Stone, J.O., Allan, G.L., Fifield, L.K. and Cresswell, R.G.: Cosmogenic chlorine-36 from
981 calcium spallation. *Geochimica et Cosmochimica Acta*, 60, 679–692, 1996.
- 982 Stuut, J.-B., Smalley, I. and O’Hara-Dhand, K.: Aeolian dust in Europe: African sources and
983 European deposits. *Quaternary International*, 198, 234–245, 2009.
- 984 Styllas, M., Pennos, C., Persoiu, A., Godelitsas, A., Papadopoulou, L., Aidona, E.,
985 Kantiranis, N., Ducea, M.N., Ghilardi, M. and Demory, F.: Aeolian dust accretion
986 outpaces erosion in the formation of Mediterranean alpine soils. New evidence from the
987 periglacial zone of Mount Olympus, Greece. *Earth Surface Processes and Landforms*, 48,
988 3003–3021, 2023.
- 989 Takahashi, Y., Chatellier, X., Hattori, K.H., Kato, K. and Fortin, D.: Adsorption of rare earth
990 elements onto bacterial cell walls and its implication for REE sorption onto natural
991 microbial mats. *Chemical Geology*, 219, 53–67, 2005.
- 992 Tesson, J., Pace, B., Benedetti, L., Visini, F., Delli Rocoli, M., Arnold, M., Aumaître, G.,
993 Bourlès, D.L. and Keddadouche, K.: Seismic slip history of the Pizzalto fault (central
994 Apennines, Italy) using in situ-produced ³⁶Cl cosmic ray exposure dating and rare earth
995 element concentrations. *Journal of Geophysical Research: Solid Earth*, 121, 1983–2003,
996 2016.
- 997 Tikhomirov D., Amiri, N.M., Ivy-Ochs, S., Alfimov, V., Vockenhuber, C., Akçar, N.: Fault
998 Scarp Dating Tool – a MATLAB code for fault scarp dating using in-situ chlorine-36
999 supplemented with datasets of Yavansu and Kalafat faults. *Data in brief*, 26, 104476,
1000 2019.
- 1001 Tesson, J. and Benedetti, L.: Seismic history from in situ ³⁶Cl cosmogenic nuclide data on
1002 limestone fault scarps using Bayesian reversible jump Markov chain Monte Carlo.
1003 *Quaternary Geochronology*, 52, 1–20, 2019.
- 1004 Tucker, G. E., McCoy, S. W., Whittaker, A. C., Roberts, G. P., Lancaster, S. T. and Phillips,
1005 R.: Geomorphic significance of postglacial bedrock scarps on normal-fault footwalls.
1006 *Journal of Geophysical Research: Solid Earth*, 116, F01022, 2011.
- 1007 Wallace, R. E.: Grouping and migration of surface faulting and variations in slip rates on
1008 faults in the Great Basin province. *Bulletin of the Seismological Society of America*, 77,
1009 868–876, 1987.
- 1010 Woodcock, N.H. and Mort, K.: Classification of fault breccias and related fault rocks.
1011 *Geological Magazine*, 145, 435–440, 2008.
- 1012 Yang, X., Liu, Y., Li, C., Song, Y., Zhu, H. and Jin, X.: Rare earth elements of aeolian
1013 deposits in Northern China and their implications for determining the provenance of dust
1014 storms in Beijing. *Geomorphology*, 87, 365–377, 2007.
- 1015 Zreda, M. and Noller, J. S.: Ages of prehistoric earthquakes revealed by cosmogenic
1016 chlorine-36 in a bedrock fault scarp at Hebgen Lake. *Science*, 282, 1097–1099, 1998.

1017 **Table 1:** Parameters for MCMC modelling of slip rate.

α (°)	β (°)	γ (°)	Scarp (cm)	Buried scarp (cm)	ρ_{rock} (g cm ⁻³)	$\rho_{\text{colluvium}}$ (g cm ⁻³)	³⁶ Cl P_o (at. g ⁻¹ yr ⁻¹)	ϵ (mm yr ⁻¹)	Pre (kyr)	Scarp age (kyr $\pm 1\sigma$)	Elapsed time (kyr $\pm 1\sigma$)
32	62	20	650	80	2.6	1.9	59.4 \pm 4.3	0.02	7.7	8.0 \pm 1.5	2.5 \pm 1.0

1018

1019 α is hanging wall colluvial surface dip angle; β is scarp dip angle; γ is the dip angle of the hillslope above the fault scarp; ϵ is
 1020 scarp erosion rate; Pre is pre-exposure; Scarp age is the initial estimate of exhumation of the oldest (highest) part of the scarp;
 1021 Elapsed time is the estimated duration following the last earthquake. The ³⁶Cl production rate of 59.4 \pm 4.3 at g⁻¹ yr⁻¹ is taken
 1022 from Schlagenhauf et al. (2010), calculated from Lifton et al. (2005).
 1023 When using the ³⁶Cl production rate of 48.8 \pm 3.5 at g⁻¹ yr⁻¹ from Stone et al. (1996), Pre is 10.6 kyr; otherwise, all other
 1024 parameters are fixed.

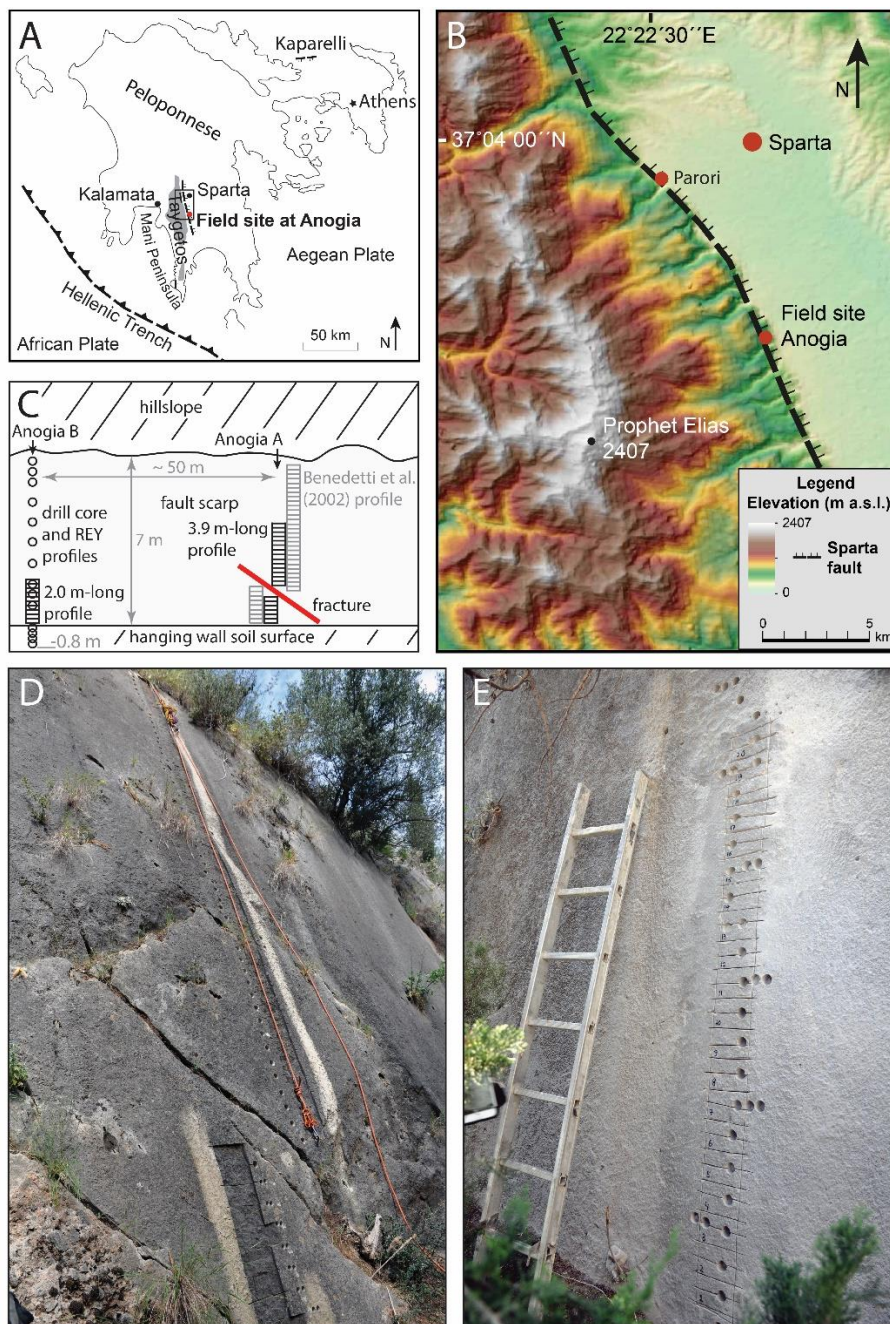
1025

1026 **Table 2:** Slip rates for the Sparta fault at Anogia from the best Markov chain Monte Carlo
 1027 models (n = 10,000), for end-member ³⁶Cl production rates and varying number of model
 1028 earthquakes.

Slip rate calculation model (³⁶ Cl production rate, number of earthquakes)	Mean slip rate (mm yr ⁻¹)	MAP slip rate (mm yr ⁻¹)
48.8, 3 earthquakes, to present	0.72	0.70
48.8, 5 earthquakes, to present	0.71	0.70
48.8, 6 earthquakes, to present	0.70	0.70
59.4, 3 earthquakes, to present	0.79	0.76
59.4, 5 earthquakes, to present	0.78	0.75
59.4, 6 earthquakes, to present	0.77	0.75
48.8, 3 earthquakes, to 464 B.C.E. earthquake	1.10	1.08
48.8, 5 earthquakes, to 464 B.C.E. earthquake	1.11	1.11
48.8, 6 earthquakes, to 464 B.C.E. earthquake	1.10	1.11
59.4, 3 earthquakes, to 464 B.C.E. earthquake	1.21	1.15
59.4, 5 earthquakes, to 464 B.C.E. earthquake	1.22	1.16
59.4, 6 earthquakes, to 464 B.C.E. earthquake	1.22	1.18
48.8, 5 earthquakes, 0–3.7 m on fault scarp	0.95	0.94
59.4, 5 earthquakes, 0–3.7 m on fault scarp	1.03	0.96
48.8, 5 earthquakes, 3.7–6.5 m on fault scarp	0.83	0.80
59.4, 5 earthquakes, 3.7–6.5 m on fault scarp	0.92	0.92

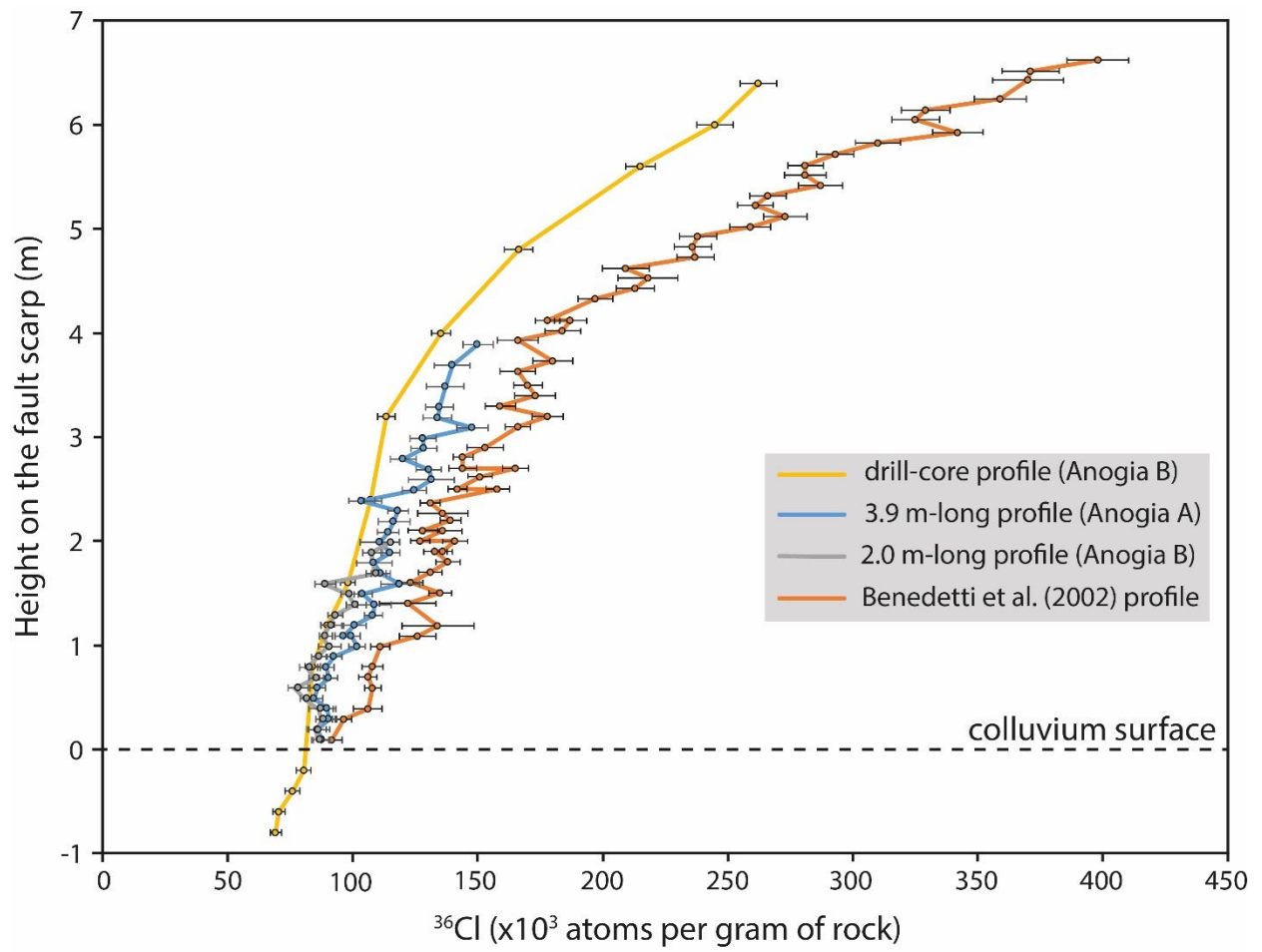
1029

MAP is maximum a posteriori probability



1031

1032 **Fig. 1:** Study site. A. The study site location in Peloponnese, Greece. Key tectonic features
 1033 are shown. Box indicates location of panel B. B. The location of the Sparta fault, separating
 1034 the Taygetos Mountains from the Sparta basin. The location of the Anogia field site used both
 1035 in this study and in Benedetti et al. (2002) is shown. Benedetti et al. (2002) located a second
 1036 sampling transect at Parori (also shown). The digital elevation model has a 24 m resolution
 1037 and is derived from ASTER GDEM (GDEM2), which is a product of NASA and METI
 1038 (Japan). C. Schematic diagram of the Sparta fault scarp at Anogia, showing the locations of
 1039 our vertical ^{36}Cl and REE-Y sampling transects, and the ^{36}Cl sampling transect of Benedetti
 1040 et al. (2002). D. Photograph showing the location of our 3.9 m-long profile, prior to
 1041 sampling. The existing sample scar is from Benedetti et al. (2002). E. Photograph showing
 1042 the location of our REE-Y and drill core profiles, after sampling, and our 2.0 m long profile,
 1043 before sampling.

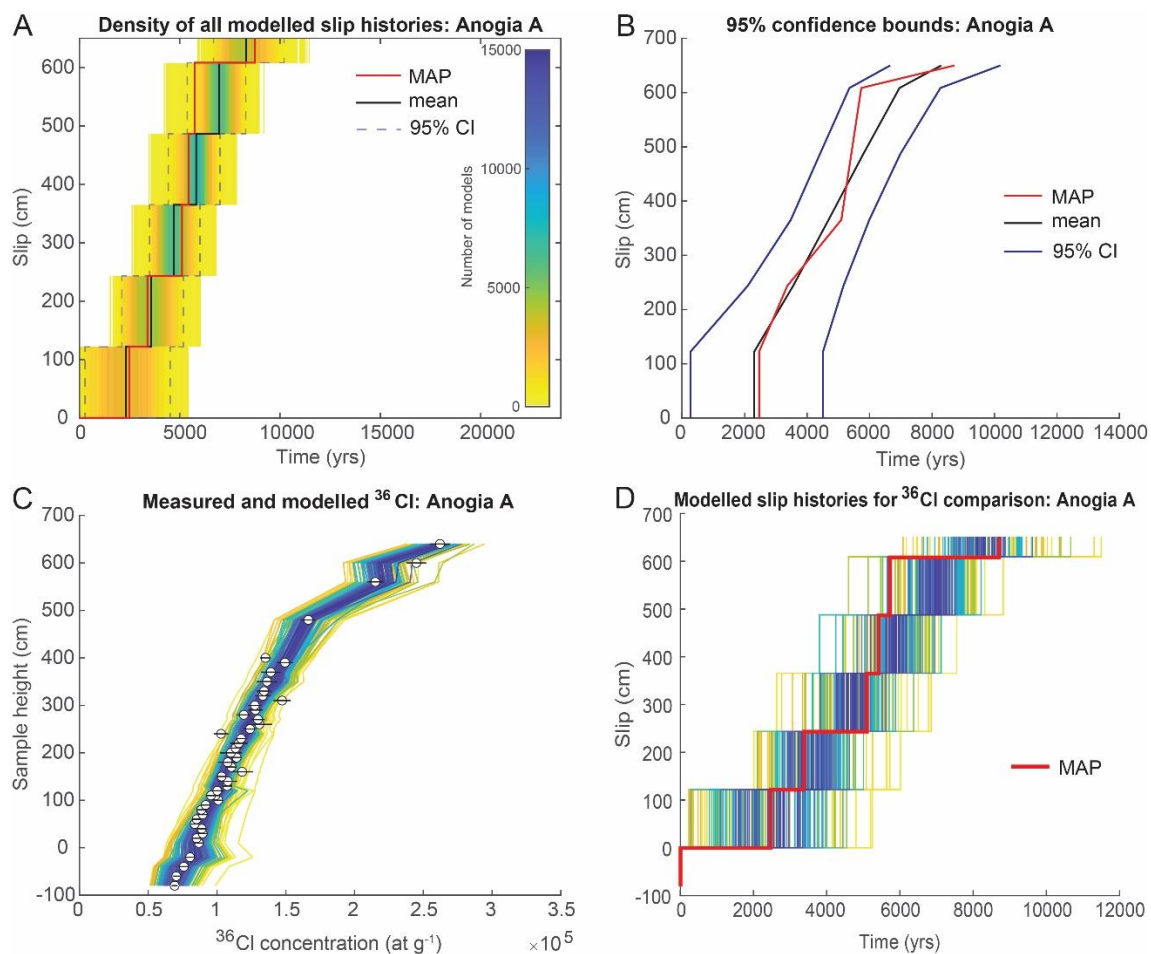


1044

1045

1046 **Fig. 2:** Sparta fault ^{36}Cl concentration profiles. Error bars indicate 1σ measurement
 1047 uncertainties..

1048



1049

1050

1051

1052 **Fig. 3:** Markov chain Monte Carlo (MCMC) model fits to measured ^{36}Cl concentrations and

1053 model slip histories, Anogia A + drill core profile. Slip accumulation is shown for five model

1054 earthquakes that each exhume the same vertical length of scarp rather than reflecting the

1055 magnitude and timing of historical earthquakes. The red line in panels a, b, and d is the

1056 maximum a posteriori probability (MAP) estimation model, which is the maximum

1057 likelihood multiplied by the prior probability based on scarp age. Each panel includes 160k

1058 iterations, following removal of a burn-in of the first 40k iterations. A. Histogram showing

1059 the distribution of accepted model slip histories in slip-space versus time. The density of

1060 overlapping models increases from warm to cool colours. The mean model and 95%

1061 confidence bounds are also shown. B. The 95% confidence bounds of the smoothed model

1062 distribution (black lines) calculated for age at each step in the slip. The mean (black line) and

1063 MAP (red line) slip histories are also plotted. C. Model fits to measured ^{36}Cl concentrations

1064 (circles). The coloured lines represent a selection of 160 model fits from low- (yellow) to

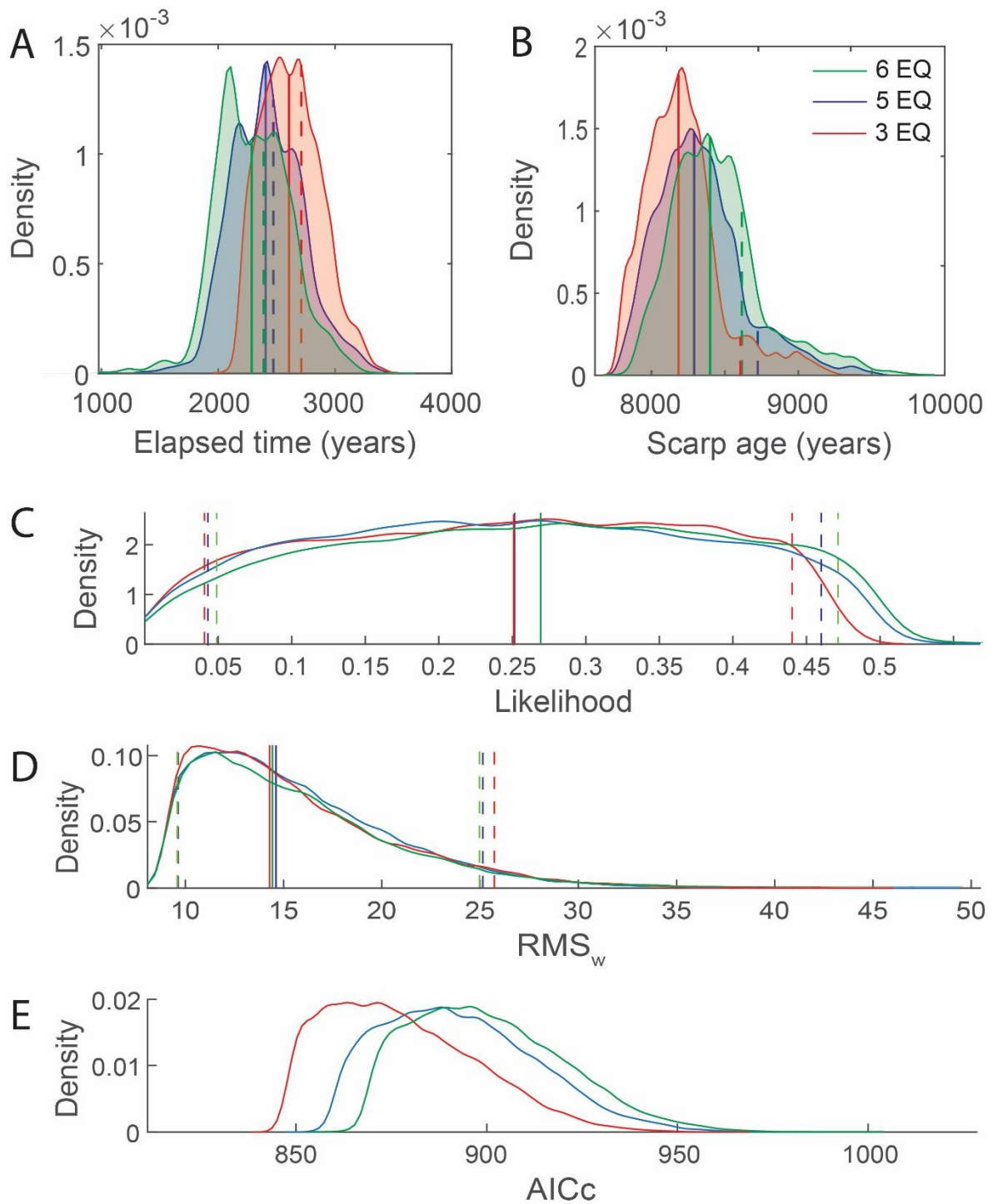
1065 high-probability (blue) at equal intervals (1000) through the distribution. The black lines

1066 indicate 1σ measurement uncertainties. D. Slip histories through five model earthquakes

1067 corresponding to MCMC fits shown in panel c. Results are shown for a ^{36}Cl production rate

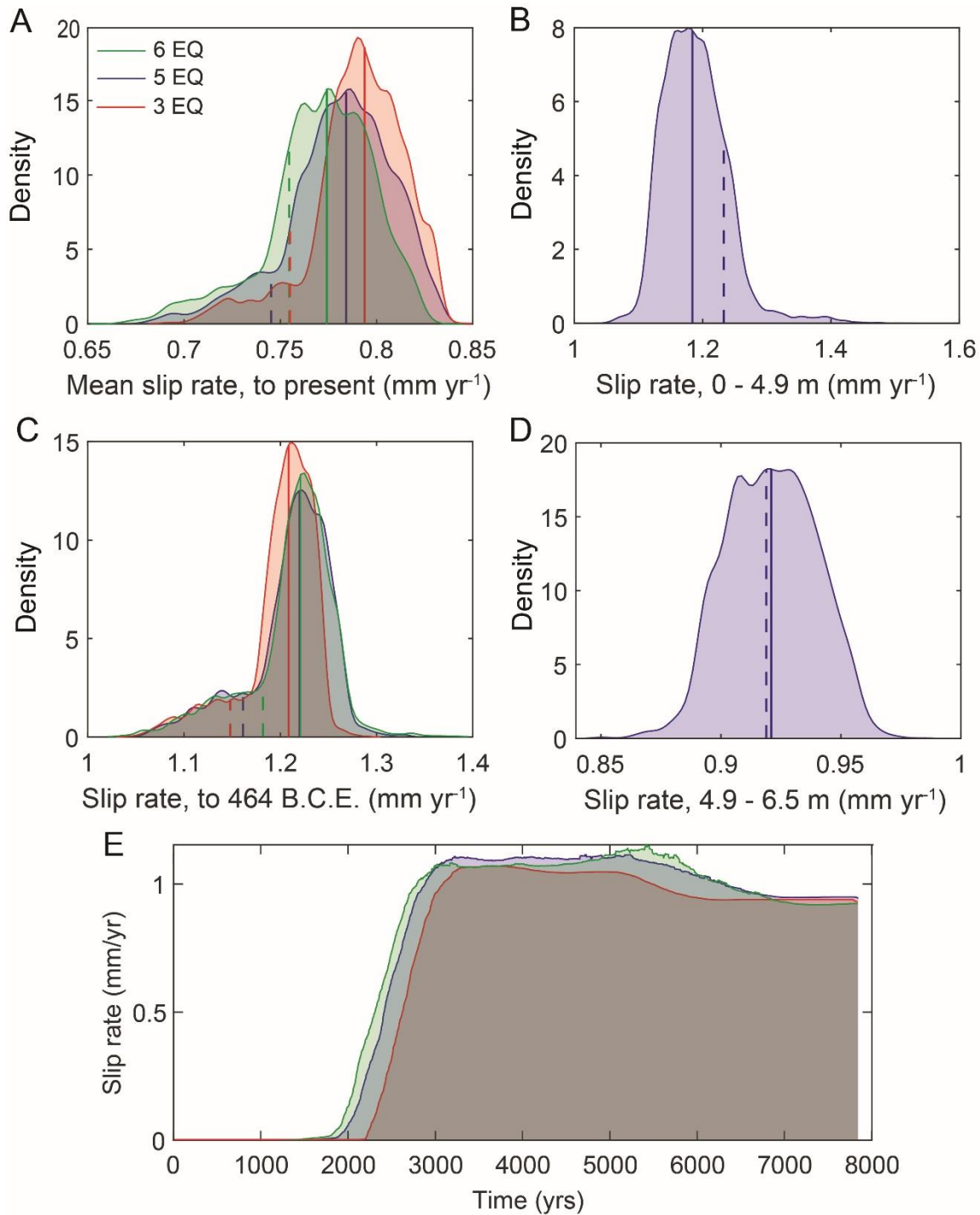
1068 of 59.4 ± 4.3 atoms $\text{g Ca}^{-1} \text{yr}^{-1}$. Refer to Fig. S2 for equivalent results using a production rate

1069 of 48.8 ± 3.5 atoms $\text{g Ca}^{-1} \text{yr}^{-1}$.



1070
 1071 **Fig. 4:** Statistical plots for 160k Markov chain Monte Carlo (MCMC) model iterations,
 1072 following removal of a 40k burn-in. Results are shown for three, five, and six model
 1073 earthquakes. Vertical red lines indicate the median of each distribution, whereas vertical
 1074 green lines indicate 95% confidence intervals. Posterior probability distribution functions
 1075 from all models for A. Elapsed Time, and B. Scarp Age. Distributions of C. Likelihood, D.
 1076 Weighted mean root square (RMS_w), and E. Corrected Akaike's Information Criterion (AICc)
 1077 of slip history calculated for modelled ³⁶Cl concentrations compared to the measured values.

1078



1080

1081

1082

1083

1084

1085

1086

1087

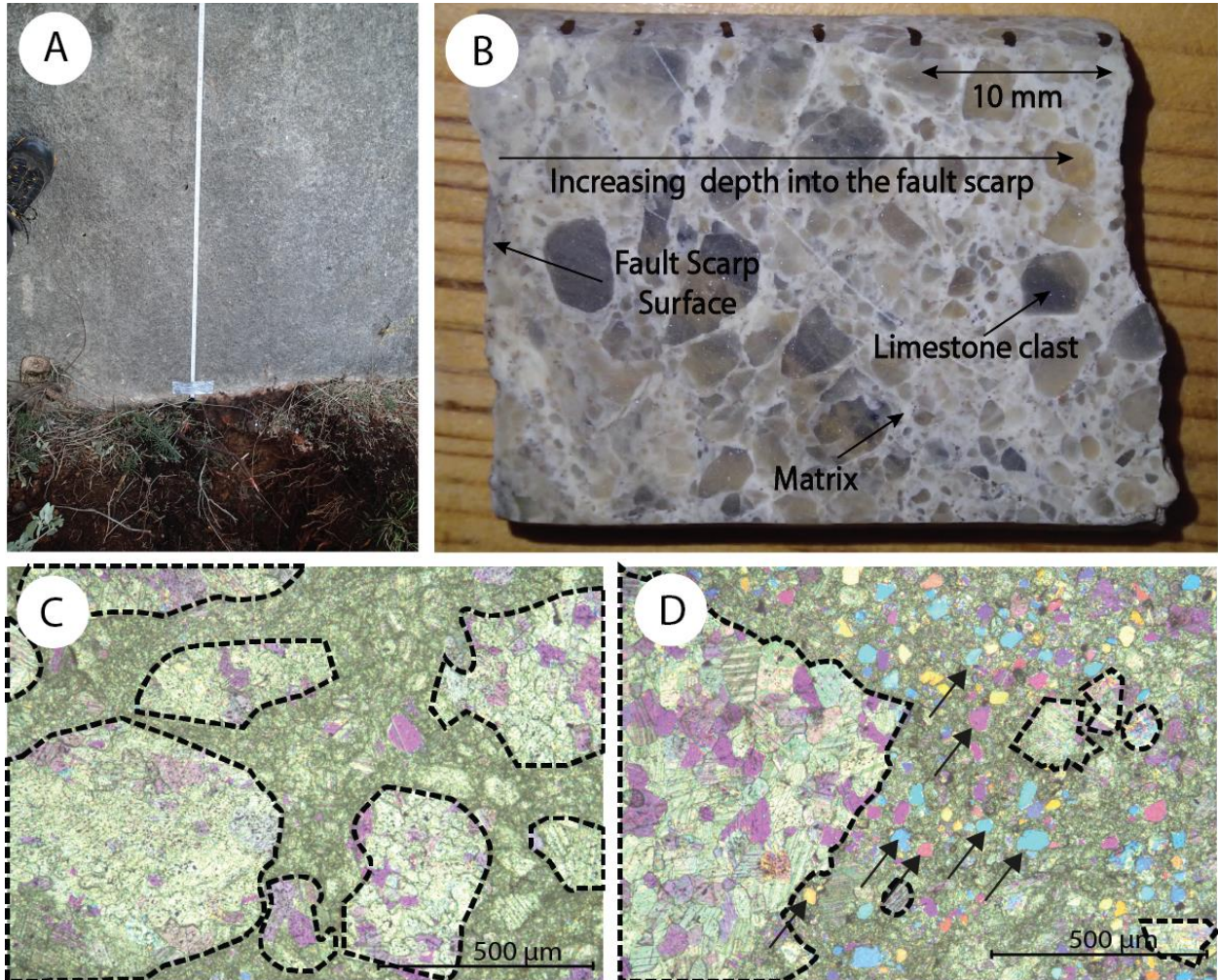
1088

1089

Fig. 5: Slip rates for the Sparta fault at Anogia (Anogia A plus drill core profile) from Markov chain Monte Carlo modelling. Results are shown for three, five, and six model earthquakes. In each panel, the most probable (top 10%) models calculated from the median scarp age and scarp height are shown. Solid and dashed vertical lines indicate the mean and maximum a posteriori probability (MAP) estimation for each distribution, respectively. Slip rates are shown for three, five, and six model earthquakes, using a ³⁶Cl production rate of 59.4 ± 4.3 atoms g Ca⁻¹ yr⁻¹. A. The distribution of the most probable slip rate for the entire scarp calculated up to the present day. B. The distribution of the most probable slip rate for the entire scarp calculated up to the last known earthquake at 464 B.C.E. C. The distribution

1090 of the most probable slip rate for lower segment of the scarp. D. The distribution of the most
1091 probable slip rate for the uppermost segment of the fault scarp. E. Mean slip rate over time.
1092 Slip rates using a ^{36}Cl production rate of 48.8 ± 3.5 atoms $\text{g Ca}^{-1} \text{yr}^{-1}$ are shown in Fig. S2.

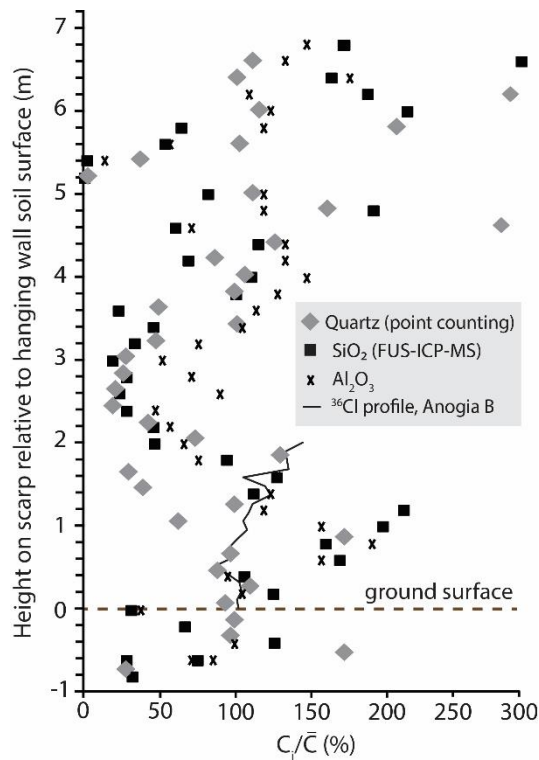
1093
1094



1095

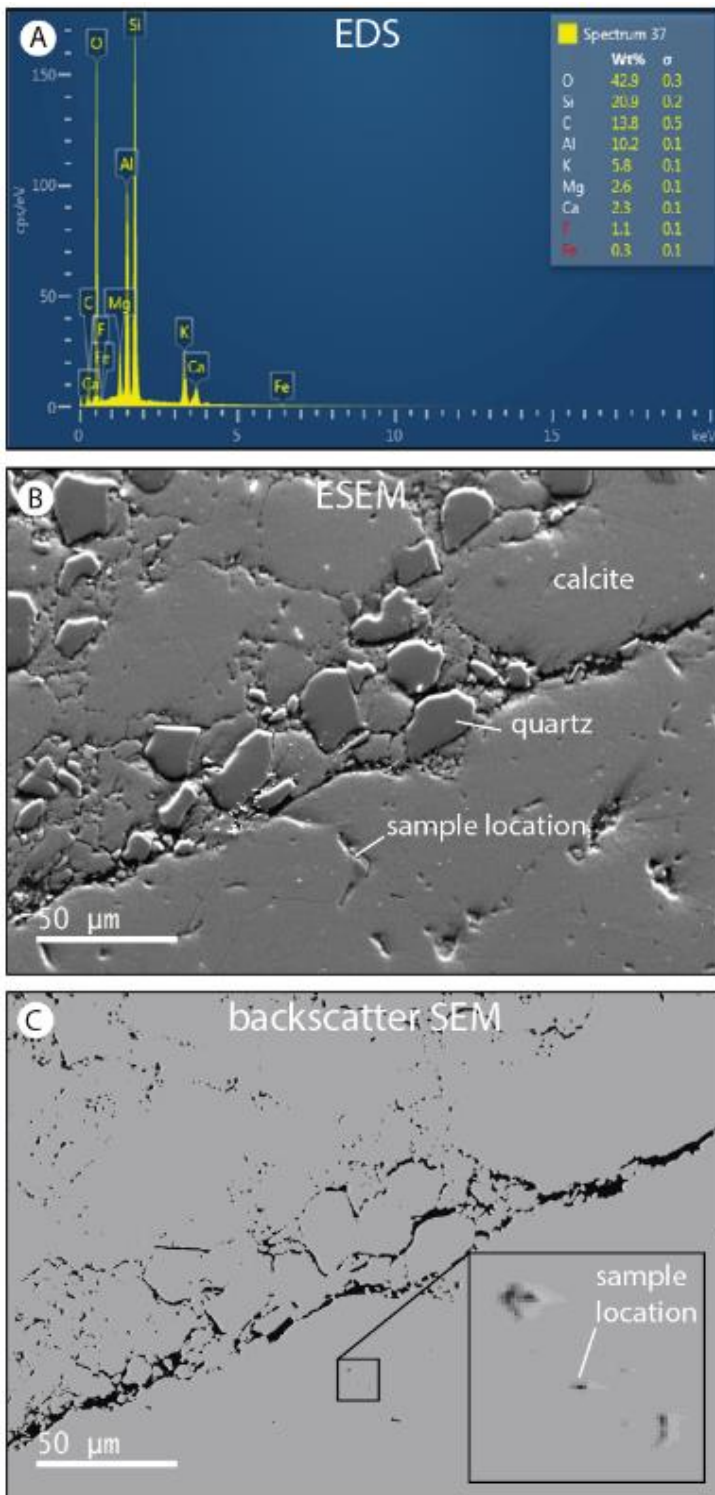
1096 **Fig. 6:** The heterogeneous fault breccia that comprises the Sparta fault scarp surface. A. The
1097 Sparta fault scarp surface appears smooth and homogenous, as illustrated by this photograph
1098 of the scarp base at Anogia (upper half of the dug trench in the foreground). B. Fault breccia
1099 is revealed in a cut drill core, where clasts of host limestone are cemented in a fine matrix. C.
1100 A photomicrograph shows limestone clasts (dotted outlines) comprising about 60% of the
1101 thin section area. D. A photomicrograph shows fine matrix comprising about 60% of the thin
1102 section area. Arrows indicate quartz.

1103



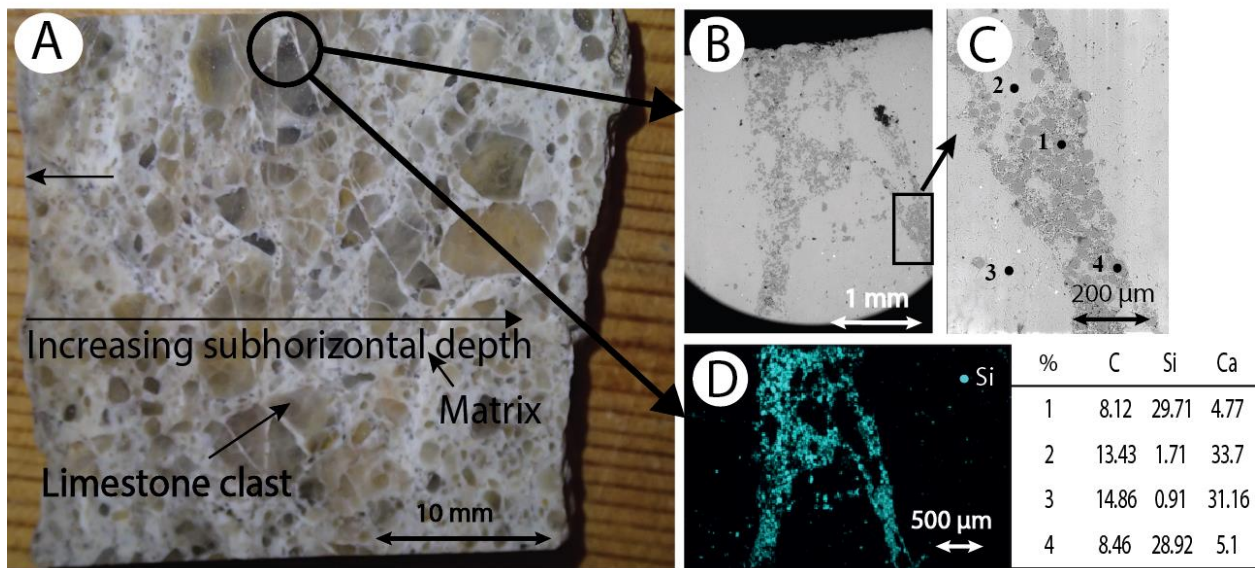
1104
 1105
 1106
 1107
 1108
 1109

Fig. 7: Concentrations of Al_2O_3 and SiO_2 , and quartz abundances from point counting, along a vertical profile, Sparta fault scarp, Anogia. The concentration of each element (C_i) is normalized to its mean concentration through the profile (C_i/\bar{C}). The locations of former soil surface horizons inferred from ^{36}Cl concentrations and from the scarp geochemistry are shown for reference.



1110
 1111 **Fig. 8:** Energy-dispersive X-ray spectroscopy (EDS) elemental abundances, and
 1112 environmental scanning electron microscope (ESEM) and backscatter SEM imagery of a thin
 1113 section of fault breccia comprising the Sparta fault scarp surface at 1.1 m above the hanging
 1114 wall. (A). Element abundances in a pore, the location of which is shown in panels B and C.
 1115 Si, Al, and K are abundant relative to Ca, which indicates that clay, e.g., illite, is lining the
 1116 pore. (B) Quartz is an abundant constituent of the thin section matrix. (C) Porosity, shown in
 1117 black; note its spatial association with quartz. The location of the sample used in panel A is in
 1118 a small pore, shown in the inset.

1119



1120

1121

1122

1123

1124

1125

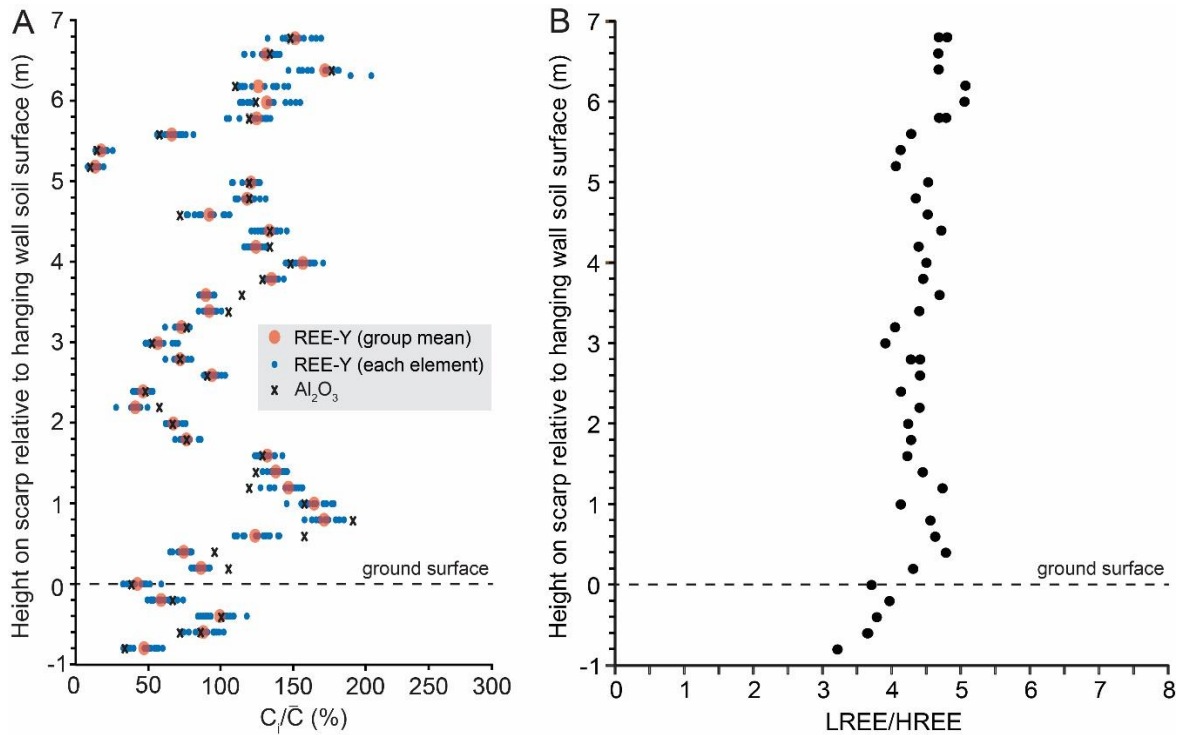
1126

1127

1128

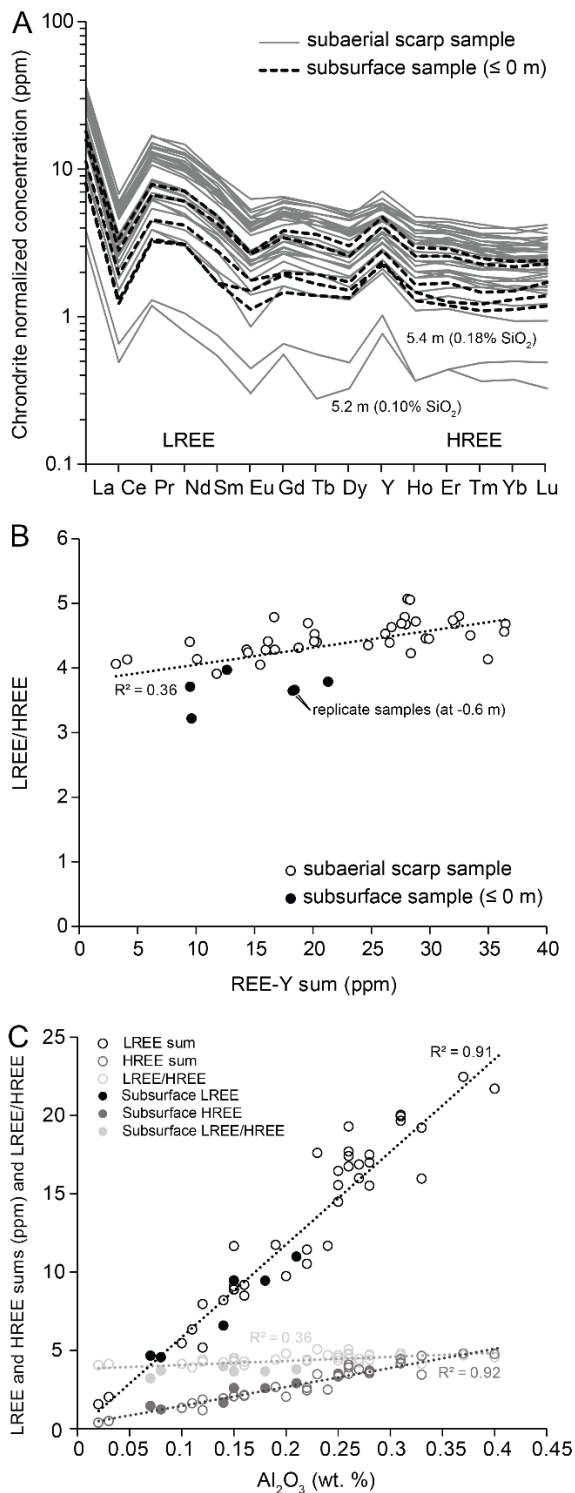
1129

Fig. 9: Concentrations of Si in the Sparta fault breccia, 1.1 m above the scarp base at Anogia. A. A cut drill core from the Sparta fault scarp at Anogia showing limestone clasts cemented in fine matrix. The circled fine matrix is examined under high resolution in panels B to D. B. An ESEM image showing the sample location for spot elemental analysis (rectangle). C. Sample points for elemental analysis using EDS, with values shown in the table. D. The abundance of Si in the fine matrix illustrated in magenta for the circled part of the thin section shown in panel A.



1130
 1131
 1132
 1133
 1134
 1135
 1136
 1137
 1138
 1139
 1140
 1141

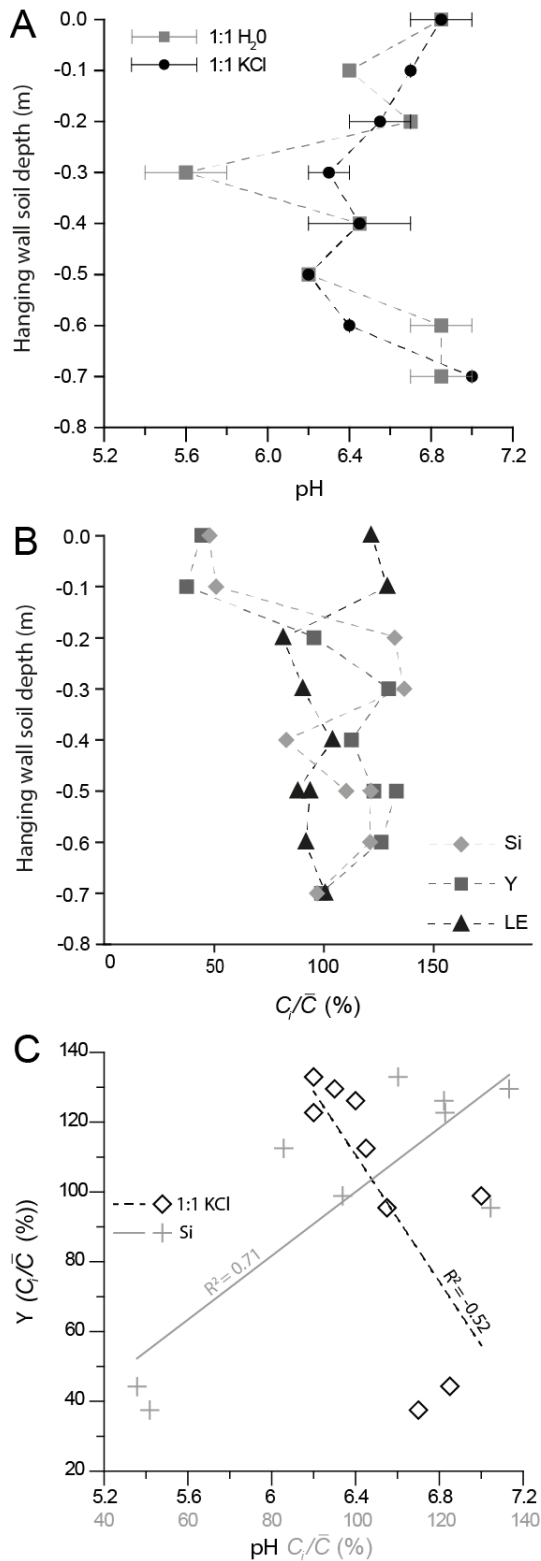
Fig. 10: Vertical distribution of REE-Y elements on the Sparta fault (Anogia B profile). A. REE-Y concentrations.. Mean values for all REE-Y elements at each sample point are shown in red dots, whereas individual REE-Y elements are shown in blue dots. The concentration of each element (C_i) is normalized to its mean concentration through the profile (C_i/\bar{C}). Concentrations of Al_2O_3 and former soil surface horizons inferred from ^{36}Cl concentrations profiles and geochemical data, are shown for reference. B. LREE:HREE ratio. There are two measurements at -0.6 m.



1142
 1143
 1144
 1145
 1146
 1147
 1148
 1149
 1150

Fig. 11: REE-Y elements on the Sparta fault (Anogia B profile). A. Concentrations of rare-earth elements and yttrium (REE-Y) normalized to chondrite composition (McDonough and Sun, 1995). Each line shows a measured location on the scarp surface. The two low REE-Y outliers at 5.2 m and 5.4 m also have exceptionally low SiO_2 and Al_2O_3 . B. LREE:HREE versus REE-Y sum. The R^2 value is for a linear fit. C. LREE, HREE, and LREE:HREE versus Al_2O_3 (wt.%). The R^2 values are for linear fits. In each panel, the six subsurface samples (≤ 0 m), including a replicate measurement at -0.6 m.

1151



1152

1153

1154

1155

1156

1157

1158

1159

Fig. 12: Hanging wall soil chemistry, adjacent to the Sparta fault scarp at Anogia. A. Soil pH along a vertical profile measured from soil mixed with distilled H₂O and 1M KCl. Uncertainty ranges show the ≤ 0.5 resolution of the indicator strips. B. Concentrations of Si, Y, and elements too light to be measured using handheld XRF (LE, including C) along the vertical soil profile. Each element has been normalized through division by its mean concentration through the soil. C. Y concentrations plotted against pH (measured from 1:1 KCl) and Si concentration at each measured depth interval beneath the soil surface.